POLARIZATION INDEPENDENT THERMO-OPTIC MODULATORS FOR INTEGRATED OPTICS

A THESIS
SUBMITTED TO THE DEPARTMENT OF PHYSICS
AND THE INSTITUTE OF ENGINEERING AND SCIENCE
OF BİLKENT UNIVERSITY
IN PARTIAL FULFILLMENT OF THE REQUIREMENTS
FOR THE DEGREE OF
MASTER OF SCIENCE

By

Aşkın Kocabaş

September 2003

I certify that I have read this thesis and that in my opinion it is fully adequate, in scope and in quality, as a dissertation for the degree of Master of Science.

Prof. Atilla Aydınlı (Supervisor)

I certify that I have read this thesis and that in my opinion it is fully adequate, in scope and in quality, as a dissertation for the degree of Master of Science.

Assoc. Prof. Ahmet Oral

I certify that I have read this thesis and that in my opinion it is fully adequate, in scope and in quality, as a dissertation for the degree of Master of Science.

Asst. Prof. Soner Kılıç

Approved for the Institute of Engineering and Science:

Prof. Mehmet Baray,
Director of Institute of Engineering and Science

Abstract

POLARIZATION INDEPENDENT THERMO-OPTIC MODULATORS FOR INTEGRATED OPTICS

Aşkın Kocabaş
M. S. in Physics
Supervisor: Prof. Atilla Aydınlı
September 2003

In this work, we studied MMI and Y-junction based Mach-Zehnder modulators on both silicon-on-insulator and polymer based on thermo-optic effect. Both P_π values and frequency response of the devices were measured and found to be consistent with those observed in the literature as well as results obtained from finite element simulations. We feel that our BCB based Y-junction modulators have the highest reported 3 -dB cut-off frequency to date. We also observe that all of our devices are polarization independent, an important feature for applications in optical communications.

Keywords: Thermo-optic modulators, Thermo-optic effect, Finite element method, Multi-mode interference, Y-junction modulator, Polymer modulator.

Özet

TÜMLEŞİK OPTİK UYGULAMALARI İÇİN KUTUPSAL OLMAYAN ISIL OPTİK KİPLEYİCİLER

Aşkın Kocabaş
Fizik Yüksek Lisans
Tez Yöneticisi: Prof. Atilla Aydınlı
Eylül 2003

Bu tezde, ısıl optik etkiye dayanan, MMI ve Y-eklem çiftleyicilere dayalı silisyum ve polimer kipleyiciler çalışıldı. Kipleyicilerin P_π değerleri ve frekansa göre tepkileri ölçüldü, ve elde edilen değerlerin hem sonlu eleman metoduyla elde edilen benzeşim sonuçları hem de bilimsel yazındaki değerlerle uygun olduğu görüldü. Polimer kipleyici için bulunan 3-dB kesim değerinin şu ana kadar ölçülmüş en yüksek değer olduğu gözlendi. Bu kipleyicilerin kutupsal olmadıkları da gözlendi.

Anahtar sözcükler: Isıl-optik kipleyici, Isıl-optik etki, Sonlu elemanlar metodu, Çok kipli girişim, Y-eklem kipleyici, Polimer kipleyici.

Acknowledgement

I would like to express my deepest gratitude to Prof. Atilla Aydınlı for his guidance, moral support, friendship and assistance during this research.

I would like to thank my twin brother Coşkun for his help that has been invaluable for me.

I would like to thank İmran AKÇA for her help during optical measurements and especially for FEM Simulations of thermo-optic devices.

I would like to thank İsa Kiyat his help for optical measurements and design of the MMI devices.

I would like to thank Feridun Ay for DPM measurements and critical reading of the manuscript.

I would like to thank Asst. Prof. Soner Kılıç for his guidance in preparing the polymer films.

I would like to thank to all Integrated Optics Group members Selcen Aytekin, Hasan İşlek, Mahmut Demir, and Nuh Sadi Yüksek for their friendship and to keep my sprits high.

Turgut Tut, Ayhan Yurtsever, Sinem Binicioğlu, Ertuğrul Çubukçu, Engin Durgun, Deniz Çakir, Cem Sevik, Ercan Avcı, Mustafa Kesir, Süleyman Tek, Necmi Bıyıklı helped to keep my spirits high all the time which I appreciate very much.

I am indebted to my family for their continuous support and care.

Contents

Abstract **i**

Özet **iii**

Acknowledgement **v**

Contents **vi**

List of Figures **viii**

List of Tables **xi**

1 Introduction **1**

1.1 Electroabsorption Modulators 1
1.2 Coupled Waveguide Modulators 2
1.3 Interferometric Modulators 3
1.3.1 Electro-Optic Effect 4
1.3.2 Acousto-Optic Effect 4
1.3.3 Free Carrier Injection Effect 4
1.3.4 Thermo-Optic Effect 5
1.4 Thermo-Optic Waveguide Materials 6

2 Elements of Thermo-Optic Modulation **8**

2.1 Thermo-Optic Effect 8
2.2 Heat Transfer in Solids 10

2.3 FEM Simulation of Heat Transfer in Thermo-Optic Devices 14

3 Thermo-Optic Multi-Mode Interference Modulators 17

3.1 Design of Single Mode Waveguides 17

3.2 Optical Multi-Mode Interference Couplers 20

3.3 Multi-Mode Interference Modulator 24

4 Thermo-Optic Y-Junction Mach-Zehnder Modulators 43

4.1 Y-junction Coupler 43

4.2 Thermo-Optic MZI Modulator 44

4.2.1 Silicon Based Thermo-Optic Modulator 46

4.2.2 Polymer Based Thermo-Optic Modulator 49

5 Conclusions and Suggestions 62

List of Figures

2. 1 Oscillations of temperature caused by periodic boundary conditions in a material with different thermal properties. 13
2. 2 Simulation steps in FEM (a)Drawing (b)Meshing (c) Solution. . . 16
3. 1 Different types of optical waveguides 18
3. 2 EIM analysis of a rib waveguide 18
3. 3 Schematic diagram of MMI coupler. 20
3. 4 Example of amplitude normalized lateral field profiles corresponding to step-index multi-mode waveguide. 21
3. 5 a)Multi-mode waveguide showing the input field, mirrored single image, a direct single image, and two fold images. b)BPM simulation of multi-mode waveguide to illustrate the image formation. 22
3. 6 Schematic diagram of MMI modulator. 25
3. 7 BPM simulation of MMI modulator for off (a) and on state (b). . 26
3. 8 Sidewiev of MMI modulator 27
3. 9 Single mode condition for different Si top layer thicknesses. For H=4 um, waveguide width of 3 um requires the etch depth to obtain the rib as 1.4 um 28
3. 10 (a)Schematic diagram of waveguide structure, (b) TE fundamental mode shape for Si ridge waveguide as calculated by BPM. 29
3. 11 2D steady state temperature distribution of the MMI modulator. The power applied to the electrode is 114 mW, ... 30

3. 12 Simulation results of pulse response when 1 kHz square wave is applied to electrode. (a)applied power (b)temperature response (c)output light intensity. 31
3. 13 Simulation result for modulation depth of output light intensity as a function of frequency. 32
3. 14 All Patterning steps of SOI optical waveguides, (a)SOI structure, (b)Si_3N_4 Deposition, (c)Photoresist Spinning, (d)Photolithography, (e)HF Etching, (f)KOH Etching, (g)Removing Si_3N_4 34
3. 15 Trench patterning steps of SOI optical waveguides (a) Si MMI waveguide, (b) Si_3N_4 Deposition, (c) Defining trench pattern, (d) KOH Etching, (e) Removing Si_3N_4, (f) SEM photograph of MMI modulator 36
3. 16 Electrode metallization of thin film heaters (a) Patterned Si waveguide, (b) Spinning PR, (c) Defining heater, (d) Al evaporation, (e) Liftoff, (f) Top view optical microscope photograph of heaters and electrodes. 37
3. 17 Optical measurement setup. 39
3. 18 View of TE_0 mode as captured with IR camera. 39
3. 19 Normalized output light intensity as function of applied electrical power. 40
3. 20 Measured normalized pulse response when a square-wave voltage pulse with a 1KHz was applied. 40
3. 21 Normalized modulation depth as a function of frequency. 42
4. 1 Schematic diagram of MZI coupler. 44
4. 2 Schematic diagram of adiabatic transition. 44
4. 3 Schematic diagram of MZI modulator. 46
4. 4 Schematic diagram of MZI structure used in modulator 46
4. 5 Simulated 2D temperature profile of MZI. 47
4. 6 Simulated temperature response for MZI. 48
4. 7 Fabrication steps for MZI 49

4. 8 Schematics of polymer device structure and FEM simulation of temperature distribution. 51
4. 9 Schematic representation of of a prism coupler setup.. 53
4. 10 Experimental setup for measuring the coupling angles. The laser beam is incident on the coupling prism. The prism coupler setup is mounted onto a high precision rotary stage with stepper motors with a precision of better that $\pm$ 0.01^o 54
4. 11 Schematics of BCB monomer. 55
4. 12 Infrared spectrum of BCB film, at%45 ,%70 and hardcured 56
4. 13 Fabrication procedure of polymer waveguide,(a) Cleaned silicon substrate, (b) PECVD SiO_2 deposition, (c) BCB Spinning, (d) Photoresist spinning, (e) Photolithography, (f) RIE Etching, (g) Removing PR 57
4. 14 View of TE_0 mode of Si based Y-junction MZ modulator as captured with IR camera. 59
4. 15 (a) Output intensity as a function of power. (b)Modulation depth vs. frequency for Si based MZI 59
4. 16 View of TE_0 mode of polymer based Y-junction MZ modulator as captured with IR camera. 60
4. 17 (a) Output intensity as a function of power. (b)Modulation depth vs. frequency for polymer based MZI. 60

List of Tables

1.1 Applications for optical switches and their switching time requirements. 5
1.2 Comparison of different optical modulators with respect to their switching time. 6
3.1 PECVD process parameters for Si_3N_4 growth. 33
3.2 Process Parameters for SiO_2. 36
4.1 Properties of used waveguide materials. 52
4.2 Process Parameters BCB RIE Etch. 58

Chapter 1

Introduction

The encoding of a signal onto an optical beam is the fundamental requirement of optical communications. There are two common methods; direct modulation of the optical source or external modulation of the optical signal.

It is difficult to modulate the semiconductor lasers at frequencies above a few GHz due to chirp [1]. And also it is difficult to operate the laser in single-mode condition at high frequencies [2]. Multi-mode lasers create pulse spreading due to dispersion because of its large spectral bandwidth. On the other hand, external modulation offers several advantages such as the fact that inexpensive continuous wave laser can be used as optical sources and different controlling mechanisms can be used in external modulators. Because of these properties external modulators take great importance in integrated optics. Generally speaking, external modulators can be classified into three different categories according to their modulating mechanism; Electroabsorption modulators [3], coupled-waveguide modulators [4], and interferometric modulators [5].

1.1 Electroabsorption Modulators

This type of modulator is based on the Franz-Keldysh effect, in which the absorption edge of a semiconductor shifts in the presence of an electric field. Applying the large electric field to the semiconductor shifts the absorption profile towards long wavelengths. For example, in GaAs, the absorption coefficient is 10 cm^{-1} for wavelength λ=0.9 μm with no electric field on the sample. If an electric field of 10^5 V/m is applied the coefficient will increase to approximately 600 cm^{-1}. The total absorption of the light depends on the path length so the transmitted signal goes as

$$I(z) = I_0 e^{-\alpha z} \tag{1. 1}$$

and the ratio is

$$\frac{I_{max}}{I_{min}} = \frac{e^{-\alpha_1 z}}{e^{-\alpha_2 z}} \tag{1. 2}$$

so a modulation depth of 20 dB can be achieved [23].

1.2 Coupled Waveguide Modulators

Coupled waveguide modulator relies on the mode coupling between adjacent waveguides. Two identical waveguides are coupled over a distance L, with electrodes placed over the waveguides to change the local index. The coupling between these two waveguides can be tuned by changing the refractive index of the waveguide. If the phase match between two waveguides is perfect then the power will transfer to the other waveguide. So by changing the refractive index the phase match can be tuned and the power transfer can be controlled. The power transferring to the other waveguides make these devices used in 1×N coupler which means one input and N outputs. Because of the difficulties in the fabrication of this kind of devices, perfect coupling is hard to achieve. The best reported modulation depth is 17 dB. In addition to this, polarization sensitivity of the coupling restricts the use of this device in optical communication switching network.

1.3 Interferometric Modulators

Interferometric modulators convert the phase modulation to intensity modulation through constructive interference between two waves. Fabry-Perot modulators, Mach-Zehnder modulators represent two examples of these kinds of modulators. In Fabry-Perot modulators, two mirrors are separated by the gap or dielectrics. Transmission through the Fabry-Perot is maximum when the optical path length between the mirrors is equal to integer number of a half wavelength. The output intensity change can be tuned by controlling the optical path via changing the refractive index or changing the length of the mirror separation. In Mach-Zehnder interferometers, light is split into two different paths and then interfere at output port. The output intensity depends on the phase shift between these two interfering beams. By creating phase shifts in one of the arms, intensity can be controlled. Phase shift can be created by changing the local refractive index. In order to change the refractive index, there are different mechanisms which depend on the material properties.

The microscopic process of polarization determines the effect a dielectric material has on light propagating through it. The material consists of the slightly separated positive and negative charges. The localized charge separation are called dipole moments. These microscopic dipole moments add to produce a macroscopic dipole moment per unit volume P. Most material can be regard as optically linear for small electric field then the polarization is proportional to electric field E as,

$$P = \chi \epsilon_0 E \tag{1. 3}$$

where the D is the electric displacement vector, χ is the dielectric susceptibility, ϵ_0 is the permittivity then we can write that

$$D = \epsilon_0(1 + \chi)E = \epsilon_0 E + P = \epsilon_0 n^2 E \tag{1. 4}$$

Therefore the refractive index, n is determined by the microscopic dipole moments that arise in response to an electric field. There are also different kinds of source of dipole moments such as ionic polarizability, free carrier polarizability and electronic polarizability. So all mechanisms which change the microscopic dipole moment can change the refractive index of the material. Mainly, electro-optic effect, acousto-optic effect, free carrier injection, and thermo optic effect have been used to control the refractive index change [6].

1.3.1 Electro-Optic Effect

The electro-optic effect has been widely used in realization for optical modulator [7]. This effect arises from anharmonic terms in the potential energy of the crystal structure. In noncentrosymmetric crystal the potential includes the nonlinear term. If the electric field is applied, the force balance equation change and results in the dc field dependent correction to the polarizability. This effect shifts the equilibrium point of the oscillating polarizability, so this change alters the polarizability and refractive index.

1.3.2 Acousto-Optic Effect

Any effects that alters the density of a material changes the polarizability as well [8]. Transverse or shear acoustic waves may change the local polarizability by altering the position of atoms relative to their neighbors. So the refractive index difference occur proportional to the local strain amplitude. The main drawback is the velocity of change. In materials, acoustic waves travel with the velocity of sound. So the speed is restricted with the sound velocity in the material.

1.3.3 Free Carrier Injection Effect

Free carrier also affect the refractive index of semiconductor. A free carrier in a semiconductor change the refractive index by band filling effect [9]. Free carriers move freely in the crystal, there is no restoring force for them, so the natural frequency is zero. The polarizability resulting from free carriers depends on the carrier density. This kind of index change is polarization insensitive but the speed is limited by the time it takes to eliminate free carriers from the semiconductor.

Application	Switching Time Required
Provisioning	1-10 ms
Protection switch	1-10 μs
Packet switching	1 ns
External modulation	10ps

Table 1.1: Applications for optical switches and their switching time requirements.

1.3.4 Thermo-Optic Effect

Thermo-optic effect stems from the temperature dependence of polarizability [10]. Temperature can change the polarization directly or it may change the material density because of the thermal expansion coefficient. The polarizability also depends on the mass density. So the temperature difference creates refractive index change.The thermo-optic effect is present in all practically used waveguide materials. The most important examples of such materials are silicon, fused silica and polymers. Thermo-optic devices receive the great attention because of their low cost fabrication and polarization independent operation in low speed optical network application.

Optical modulators are used in optical networks for a variety of applications. The main important parameter in these kinds of application is switching time which varies from few milliseconds to subnanoseconds. Table 1.1 summarize the application areas of optical modulators and their switching time requirements [11]. In provisioning the modulators are used in optical crossconnects to reconfigure them to support new light paths. So for this application modulators with millisecond switching times are acceptable. Another application is protection switching. Here the modulators are used to switch the traffic stream from one fiber to another fiber in case the primary fiber fails. The required switching times is in the range of few milliseconds to hundred microseconds. Packet switching is used in high speed application. In this network in order to switch the signal on a packet the switching time must be much smaller than the packet duration. The switching time is in the order of a nanoseconds in packet switching. Finally, in order to turn on and off the data in front of a

Type	Switching Time
Mechanical	10 ms
Thermo-optic	1 ms
Electro-optic	1 ns- 10 ps

Table 1.2: Comparison of different optical modulators with respect to their switching time.

laser source external modulation is used. In this case, the switching time must be a small fraction of the bit duration. So the external modulator must have picoseconds switching time.

1.4 Thermo-Optic Waveguide Materials

There is growing interest in the switching of light with planar optical components for applications in optical fiber telecommunications. Today, the main technology for planar modulator fabrication is Ti-diffusion in $LiNbO_3$ [12], where the switching is achieved using electro-optic effect. These components can be switched very fast, but are generally polarization sensitive and expensive. In some applications polarization insensitivity is more important than the switching speed. For example by-pass switching in LAN's with ring topology and circuit switching for video distribution. For these applications optical waveguide modulators using the polarization independent thermo-optic effect can be a good alternative. And also thermo-optic control of optical modulators is attractive from viewpoint of simplicity and low cost. The most important examples of such materials are silicon and polymers.

Silicon is the most commonly used material in electronics. Its technology is highly developed so it offers a large potential for low cost optical devices. There is no inversion symmetry in Si crystal. Since the electro-optic effect (Kerr-effect) in silicon is too small [13], only the plasma dispersion effect and the thermo-optic effect are promising candidates for the realization for optical modulators. In addition to plasma dispersion effect, high thermo-optic coefficient of Si offer a good possibility for influencing the optical wave. According to Chapter 2 only

1-5K temperature difference is sufficient for refractive index change of 2×10^{-4}.

In addition to switching time, power consumption is also important parameter for thermo-optic devices [26]. In thermo-optic modulators power consumption depends on thermo-optic coefficient and thermal conductivity [14]. In order to decrease the operating power low thermal conductivity and high thermo-optic coefficient are needed. Polymers are good candidates for this kind of application because of their low thermal conductivity. Because of easy and low cost waveguide fabrication techniques such as spin coating at low temperature polymers have received the great attention in thermo-optic modulators fabrication.

Chapter 2

Elements of Thermo-Optic Modulation

Modulation of optical output in Mach-Zehnder interferometer devices is obtained by modulating the optical path difference between the arms of the interferometer. In devices made of Si and polymers where the electro-optic effect is absent, this is done by modulating the temperature of the arms to invoke the temperature dependence of the refractive index. Local modulation of the refractive index is achieved by supplying a square wave electrical pulse train to an appropriately placed heater on one arm of the interferometer. Understanding heat transfer in these devices is, therefore, important. This chapter is devoted to theoretical background of thermo-optic devices. The origins of the thermo-optic effect in silicon and polymers will be given. Analytical and numerical methods for solution of heat transfer problem which will be used in next chapters will also be introduced.

2.1 Thermo-Optic Effect

The change in refractive index n, of a material at temperature T , is due to the change in density ρ, and due to the thermal change in polarizability. The rate of change of index with temperature $\frac{dn}{dT}$ can be written as [15]

$$\frac{dn}{dT} = (\frac{\delta n}{\delta \rho})_T(\frac{\delta \rho}{\delta T}) + (\frac{\delta n}{\delta T})_\rho \tag{2. 1}$$

or

$$\frac{dn}{dT} = -(\rho\frac{\delta n}{\delta \rho})_T\gamma + (\frac{\delta n}{\delta T})_\rho \tag{2. 2}$$

where γ is the coefficient of volume expansion of the material. From the Lorentz-Lorenz (LL) equation, The following expression for $(\frac{\rho\delta n}{\delta\rho})_T$

$$(\frac{\rho\delta n}{\delta \rho})_T = (1-\Lambda_0)\frac{(n^2+2)(n^2-1)}{6n} \tag{2. 3}$$

where Λ_0 is the strain polarizability constant that has been introduced by Muller [16] to take into account the effect of density changes on the atomic polarizability of the material. Temperature induced index changes for polymer and Si need to be calculated , separately.

For polymers, Λ_0 is small compared to unity as a consequence of weak interaction between the molecular units. For example, value of Λ_0 is 0.15 for polymethlylmethacrylate [17]. As the refractive index of most polymers is $\sim$1.55 and the thermal expansion coefficient is 2×10^{-4}, the first term of the Equation 2. 2 becomes

$$-(\rho\frac{\delta n}{\delta \rho})_T\gamma \sim -10^{-4}/^0C. \tag{2. 4}$$

The thermal change of the refractive index at constant density, that is, the second term in Equation 2. 2, is small. For example for polymethlylmethacrylate [17]

$$-(\rho\frac{\delta n}{\delta T})_\rho \sim -4\times10^{-6}/^0C. \tag{2. 5}$$

Therefore it can be concluded that the thermo-optic coefficient in polymers has a large negative value as it is determined predominantly by density change caused by the strong thermal expansion in these materials. The value of refractive index changes becomes

$$\frac{dn}{dT} \sim -(\rho\frac{\delta n}{\delta\rho})_T\gamma \sim -10^{-4}/^0C \tag{2. 6}$$

for glassy polymers.

For silicon, Λ_0 is $\sim$ 0.5 and thermal expansion coefficient has a value of 2×10^{-6}. The refractive index of silicon is $\sim$3.4 (λ =1.55μm). From Equation 2. 3 it follows that

$$-(\rho\frac{\delta n}{\delta\rho})_T\gamma \sim -4/^0C. \tag{2. 7}$$

Therefore the first term in Equation 2. 2 is of the order of

$$-(\rho\frac{\delta n}{\delta T})_\rho \sim -10^{-5}/^0C. \tag{2. 8}$$

and finally the thermal change of refractive index caused by density change can be estimated as

$$\frac{dn}{dT} \sim -(\rho\frac{\delta n}{\delta\rho})_T\gamma \sim -10^{-5}/^0C. \tag{2. 9}$$

On the other hand, the temperature dependent refractive index change of silicon is about $2\times10^{-4}/^0C$. In silicon, thermo-optic effect is mainly due to the second term of Equation 2. 2 which originates from the thermal changes in the polarizability. It can be concluded that the thermo-optic coefficient of silicon is of the same order of magnitude with polymers and its sign is positive, and opposite to that of the coefficient in polymers. The optical modulation depends on the absolute value of refractive index changes so that its sign does not effect the modulation mechanism.

2.2 Heat Transfer in Solids

Heat transfer can be defined as the transport of energy due to a temperature difference. There are mainly three distinct mechanisms by which heat transfer takes place: (i) Conduction, (ii) Convection, (iii) Radiation. In solids, convection is absent and heat transfer via radiation can be neglected for room temperatures. Therefore, conduction is the dominant heat transfer mechanism in solids [18] under our consideration.

Heat conduction in solids is due both to the excitation of the vibrational modes of atomic molecular species and the motion of free electrons. Conduction is governed by Fourier's law stated as; the rate of heat conduction ($\dot{Q}$) is proportional to the area (A) normal to the direction of the heat flow and to the temperature gradient($\frac{dT}{dx}$) in the direction of the heat flow. Thermal conductivity defined by k and has the unit of W/mK(SI). A mathematical statement of Fourier's law for 1D heat flow is

$$\dot{Q} = -A\frac{dT}{dx} \tag{2. 10}$$

or,

$$q = \frac{\dot{Q}}{A} = -\frac{dT}{dx}. \tag{2. 11}$$

Thermal analysis concerns itself with both the steady state and transient conduction of heat. Considering the principle of conservation of energy for volume element, the general heat transfer equation can be written as

$$\nabla^2 T + \frac{\dot{q}}{k} = (\frac{\rho C}{k})\frac{\partial T}{\partial t}. \tag{2. 12}$$

Where C is the heat capacity. For steady state condition without internal heat generation equation becomes;

$$\nabla^2 T = 0 \tag{2. 13}$$

and transient heat equation without internal heat generation takes the following form

$$\nabla^2 T = (\frac{\rho C}{k})\frac{\partial T}{\partial t}. \tag{2. 14}$$

Initial conditions for the differential equations specify the temperature distribution throughout the entire region at time, $t = 0$. Boundary conditions can be formulated in three different types as; first, second and third kinds. A first kind boundary condition defines the temperature on the boundary explicitly, for example T(0,t)=10 ^0C. A second kind of boundary condition defines the temperature on the boundary implicitly, in terms of heat flux. For example

$$q(L,t) = (\frac{dT}{dx})_{x=L} = -\frac{100}{k} \tag{2. 15}$$

where k is the thermal conductivity of the material. A boundary condition of third kind specifies the temperature gradient at the surface in terms of an external heat transfer coefficient h, the surface temperature T_s and the reference temperature T_{ref}, for example,

$$-k(\frac{dT}{dx})_{x=0} = h(T_s - T_{ref}). \quad (2.\ 16)$$

In thermo-optic devices, periodic boundary conditions are created by electrical heating. So, the time dependent solution of heat equation with periodic boundary conditions takes primary importance.

We seek solutions of the type

$$T = ue^{i(wt-\varepsilon)} \quad (2.\ 17)$$

substituting in the differential equation, it follows that u must satisfy

$$\frac{d^2u}{dx^2} = \frac{iw}{k}u \quad (2.\ 18)$$

so the solution of period $\frac{2\pi}{w}$ should be in the following form

$$T = Ae^{-kx}\cos(wt - \varepsilon - kx) \quad (2.\ 19)$$

when the surface temperature is a periodic function of time of period $\frac{2\pi}{w}$, we can obtain the solution by using the Fourier series for $\theta(t)$

$$\theta(t) = A_0 + A_1 cos(wt - \epsilon_1) + A_2 cos(2wt - \epsilon_2) + ... \quad (2.\ 20)$$

and if the $\theta(t)$ is the square wave with the period τ then we find the temperature [19].

$$T = \frac{4}{\pi}\sum\frac{1}{(2n+1)}e^{-x\sqrt{(2n+1)\pi/2k\tau}} sin[\frac{(2n+1)\pi t}{\tau} - x\{\frac{(2n+1)\pi}{2k\tau}\}^{\frac{1}{2}}] \quad (2.\ 21)$$

In Figure 2. 1 temperature is plotted as a function of time in which the higher harmonics disappear and square wave gradually becomes exponential and then sinusoidal as the thermal conductivity decreases and heat capacity increases. In

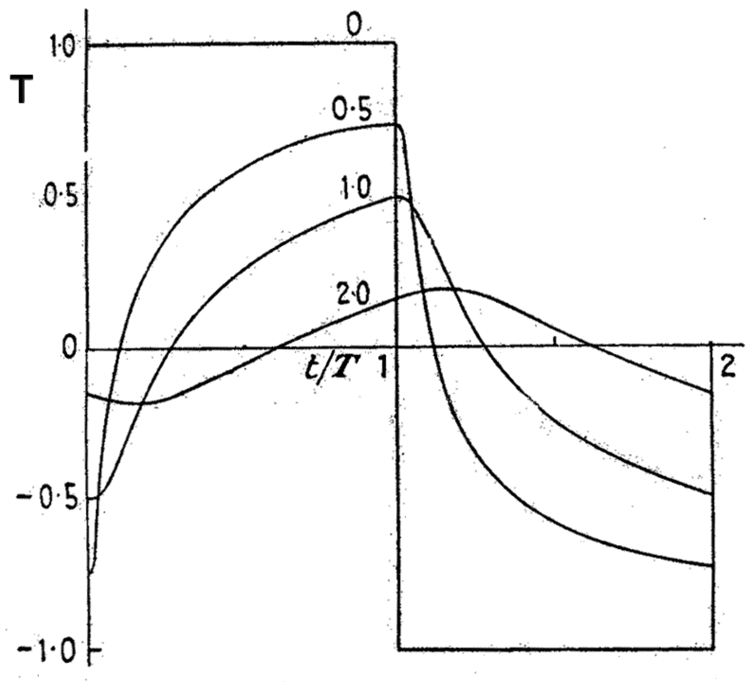

Figure 2. 1: Oscillations of temperature caused by periodic boundary conditions in a material with different thermal properties.

Figure 2. 1 each axis normalized and each curve represents the temperature response of different materials with different thermal properties .

Finally, the analogy between the theory of alternating current circuits can be noted.

$$\frac{\rho c}{k}\frac{\partial V}{\partial t} = -\frac{\partial^2 V}{\partial^2 x} \tag{2. 22}$$

$$I = -k\Omega\frac{\partial V}{\partial x} \tag{2. 23}$$

where V is potential, k is the electrical conductivity and c is the capacitance. The temperature is equivalent to potential and heat flow can be represented by current in circuit theory. The theory of electrical circuits is well known. This implies that the behavior of a complicated thermal network may be modelled by the analogy with circuit theory.

2.3 FEM Simulation of Heat Transfer in Thermo-Optic Devices

There are many engineering problems for which the exact solution for heat transfer equations can not be analytically obtained. This difficulty requires the use of numerical methods and approximations to deal with such problems. There are two common classes of numerical methods for solution of differential equations: (1) Finite difference methods, (2) Finite element methods. We have made use of the finite element method to analyze the thermal effects in optical devices. The finite element method is a numerical procedure to obtain a solution to variety of problems such as steady state and transient problems in stress analysis, heat transfer and electromagnetism. The significant step in utilization of finite element method was taken by Boeing in 1950's to model airplane wings [20].

Galerkin's method is one of the most commonly used procedures in finite element formulation. The Galerkin's method requires the error ($\Re$) to be orthogonal to the same weighting functions ϕ_i, which known as shape functions, according to the integral [20].

$$\int \phi_i \Re dy = 0 \quad (for\ i = 1, 2, ..., N) \tag{2. 24}$$

In this representation it is needed to determine the shape function according to a defined element. The first approximation is dividing the solution domain into elements. Next step, is to choose the element type and determine the shape functions. Applying the Galerkin method, the approximate solution can be found for each element, then assembly of elements leads to the global conductance matrix. By applying the boundary conditions, nodal temperature solution can be found from the final sets of linear equations.

ANSYS and FEMLAB are commercial computer programs that allow to model the physical problem with finite element analysis. FEMLAB has a powerful, interactive environment for modelling and solving scientific and engineering problems based on partial differential equations. Figure 2. 2 represents the solving procedure of FEMLAB. Drawing the geometry under consideration is the first step, in which the device geometry is defined Fig 2.2.a. Second step is meshing the area, Fig2.2.b. Through the meshing process, partial differential equation can be solved for each element as explained earlier, Fig2.2.c. After drawing and meshing steps, the required material properties and boundary conditions are defined. Finally, by running the numerical solver, the solution is obtained.

The accuracy of the solution depends on the element type and meshing size. We can improve the accuracy of finite element findings by either increasing the number of linear elements used in the analysis or using a higher order interpolation function. In linear function, two nodes are enough to define the temperature distribution through the element. For example, for 1-D linear element,

$$T^e = c_1 + c_2 X \tag{2. 25}$$

For 1-D quadratic element, the defined temperature distribution is

$$T^e = c_1 + c_2 X + c_3 X^2. \tag{2. 26}$$

Utilizing a quadratic function instead of a linear function requires that we use three nodes to define the computational element. This higher order interpolation increases the accuracy of the solution but also increases the required computational time unacceptably.

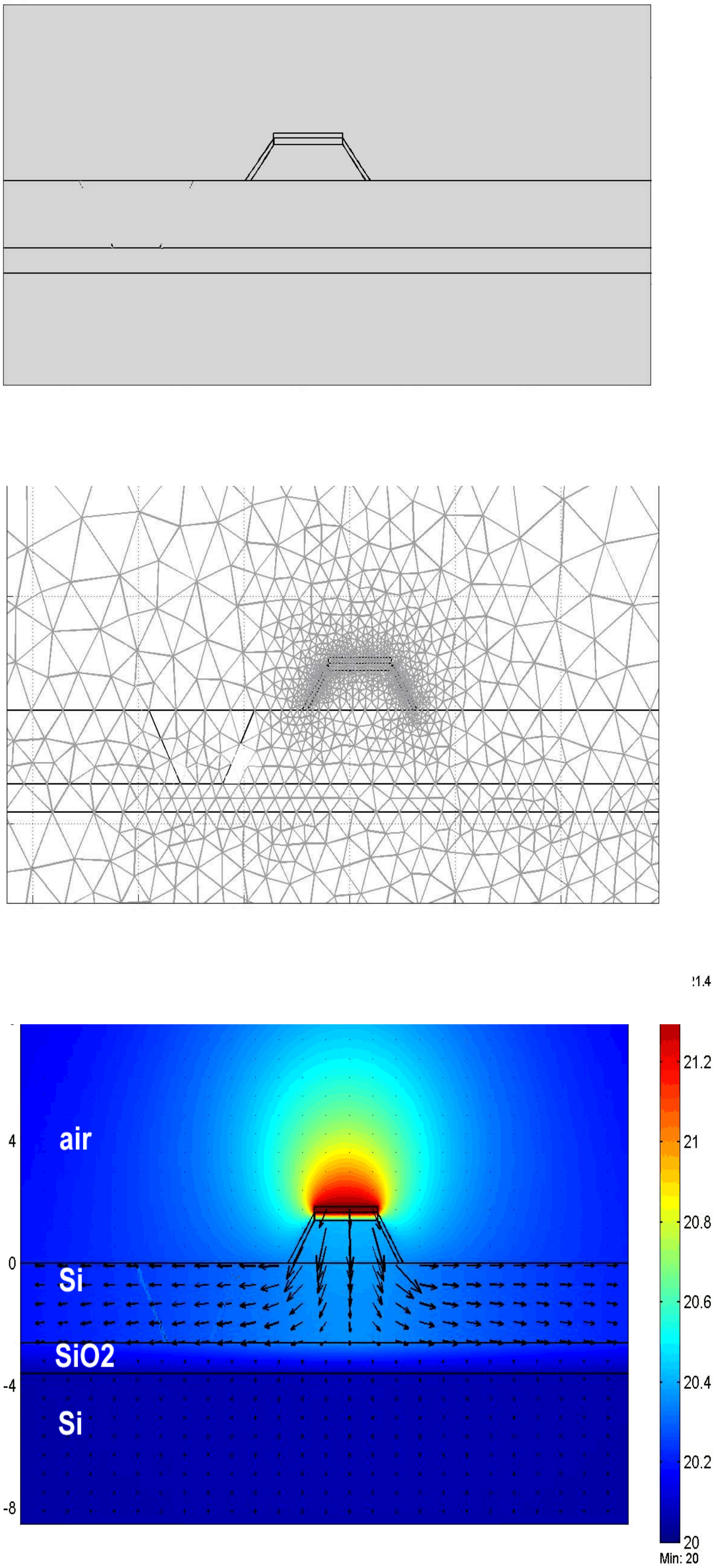

Figure 2. 2: Simulation steps in FEM (a)Drawing (b)Meshing (c) Solution.

Chapter 3

Thermo-Optic Multi-Mode Interference Modulators

In this chapter, conditions for single mode waveguide design is elaborated and theoretical background of multi-mode interference (MMI) couplers is presented. In addition to MMI coupler based thermo-optic devices design, finite element simulations of heat diffusion is discussed.

3.1 Design of Single Mode Waveguides

The design of single mode waveguides starts with the design of a slab waveguide using materials of choice as the device platform. The slab waveguides are easy to design because of their simple geometry and well defined boundary conditions. However, slab waveguides cannot confine the light in the lateral direction. For integrated optical applications, it is required to guide the light in a predefined optical path. In order to achieve vertical and lateral confinement of light dielectric rectangular waveguides are most commonly used in integrated optics.

Three possible configurations for rectangular waveguides are shown in Figure 3. 1. Analysis of this kind of waveguides is difficult because it is impossible to simultaneously satisfy all boundary condition with any analytical expression.

There are two frequently used waveguide design tools, namely effective index

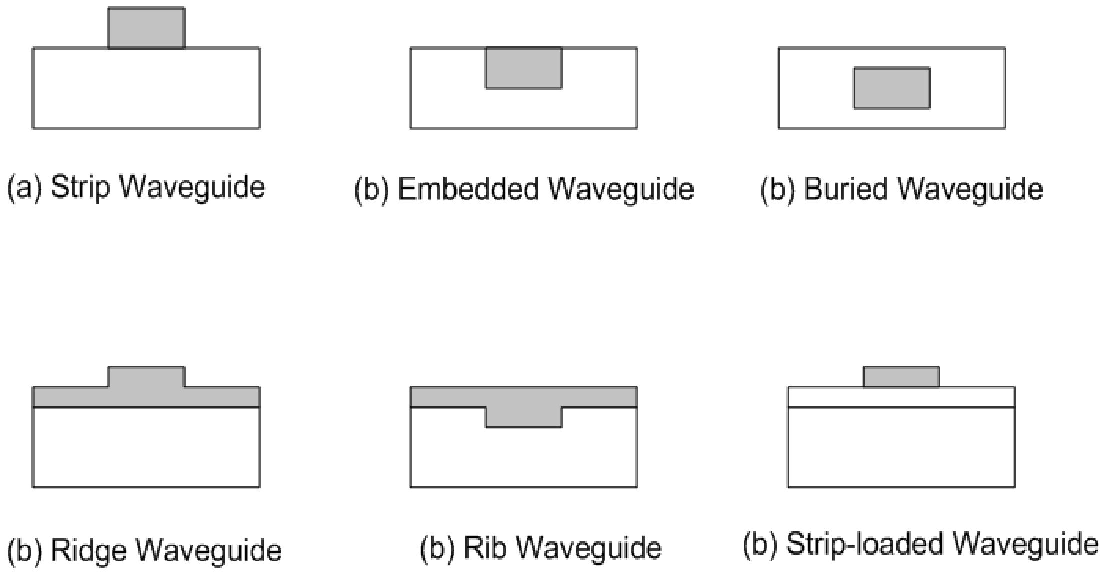

Figure 3. 1: Different types of optical waveguides

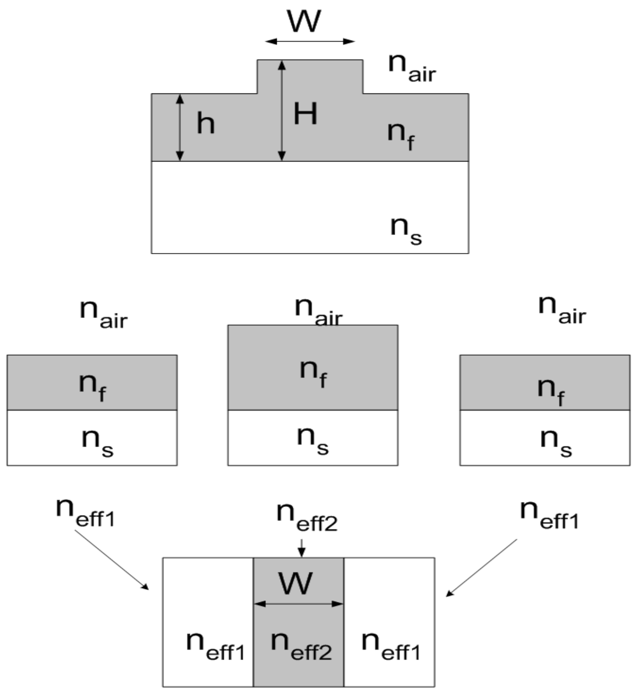

Figure 3. 2: EIM analysis of a rib waveguide

method (EIM), which is an relatively easy method useful for most of the design purposes and the beam propagation method (BPM), which is a numerical simulation technique based on finite difference solution techniques. The effective index method convert the two dimensional problem into one dimensional problem. In this method the rib waveguide is divided into three slab structures for each of which the exact solution is straightforward. The propagation constant, β for guiding mode is calculated from the eigenmode equations of the slab waveguide for two slab waveguide structures. Then effective index is calculated for each structure using,

$$n_{eff} = \frac{\beta}{\kappa_0}. \tag{3. 1}$$

Using the effective indices an artificial slab waveguide structure is formed as in Figure 3. 2 and calculation of the β is repeated for this structure using Equation 3. 1. The resulting effective index is the effective index of original rib waveguide. Finally, the single mode condition for final slab waveguide can be stated as

$$t < c + \frac{r}{\sqrt{1-r^2}} \tag{3. 2}$$

where

$$\begin{aligned} c &= 0.5 \\ t &= \frac{w_{eff}}{H_{eff}} \\ r &= \frac{h_{eff}}{H_{eff}} \\ h_{eff} &= h + q \\ H_{eff} &= H + q \\ w_{eff} &= w + \frac{2\gamma_{uc}}{k\sqrt{n_f^2 - n_{uc}^2}} \\ q &= \frac{\gamma_{uc}}{k\sqrt{n_f^2 - n_{uc}^2}} + \frac{\gamma_{lc}}{k\sqrt{n_f^2 - n_{lc}^2}} \end{aligned} \tag{3. 3}$$

and n_f,n_{uc},n_{lc} are the refractive indices of the guiding region, upper and lower cladding, respectively. After initial design using the EIM, the result can be verified by using BPM simulation by calculating the mode spectrum of the waveguide.

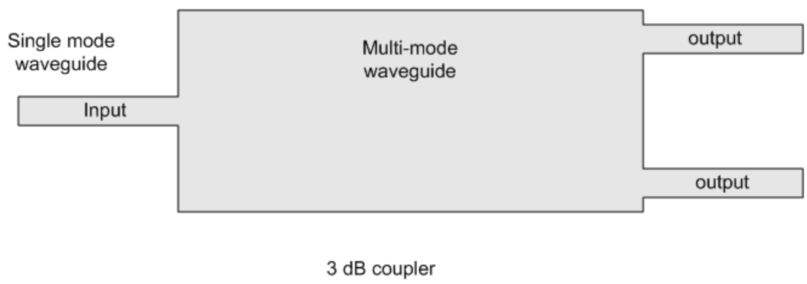

Figure 3. 3: Schematic diagram of MMI coupler.

3.2 Optical Multi-Mode Interference Couplers

In general, a MMI is a multimode waveguide that is fed by single mode waveguide(s) and allows the interference of waves diffracting at the input port(s) leading to nodes (constructive interference) and antionodes (destructive interference) at which ouput port(s) may be placed. The operation of Multi-Mode Interference (MMI) devices is based on the self-imaging principle. This principle can be stated as the property of a multi-mode waveguide by which an input field profile is reproduced in multiple images at periodic intervals along the propagation direction [21]. Figure 3. 3 illustrates the basic structure of an MMI coupler. It consists of a multi-mode waveguide and with a single mode input waveguide and two single mode output waveguides. Single mode waveguides are designed to launch or recover the light and multi-mode waveguide is designed to support a large number of modes for general interference for self imaging. In Figure 3. 3 an MMI coupler designed to split light into two output channels is illustrated. Ψ_0 is being an input field profile, and after sudden transition multi-mode region, Ψ_0 spreads into all available modes of the multimode waveguide. Typically, multi-mode waveguides are chosen to support more than 3 modes. Using the orthogonality relation we can write the field profile as

$$\Psi(y,z) = \sum c_\nu \psi_\nu(y) \exp[j(wt - \beta_\nu z)] \qquad (3.\ 4)$$

where $\psi_\nu(y)$ are all available modes and c_ν are the field excitation coefficients,

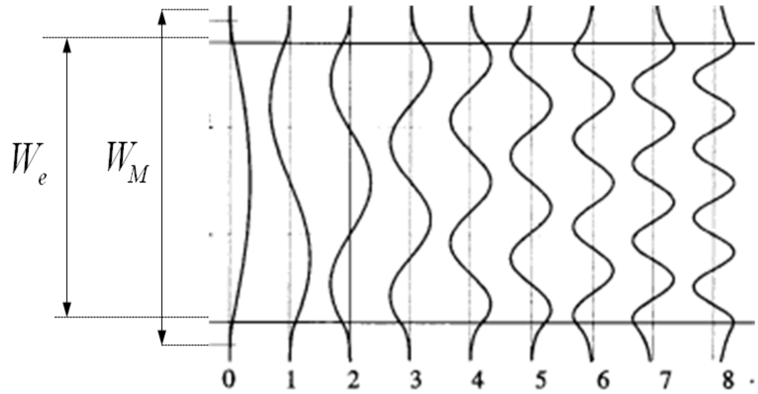

Figure 3. 4: Example of amplitude normalized lateral field profiles corresponding to step-index multi-mode waveguide.

$$c_\nu = \frac{\int \Psi(y,0)\psi_\nu(y)\ d(y)}{\sqrt{\int \psi_\nu^2 dy}}. \tag{3. 5}$$

For mode propagation analysis, modes of the waveguides should be determined. For a multi-mode waveguide of width W_M, ridge refractive index n_r and cladding refractive index n_r, and wavelength λ_0, the dispersion equation for the lateral modes can be written as

$$k_{y\nu}^2 + \beta_\nu^2 = k_0^2 n_r^2 \tag{3. 6}$$

for which $k_{y\nu}^2$ is defined as the lateral wave number for mode ν

$$k_0 = \frac{2\pi}{\lambda_0} \tag{3. 7}$$

$$k_{y\nu} = \frac{(\nu+1)\pi}{W_{e\nu}} \tag{3. 8}$$

and the propagation constants spacing can be written as

$$(\beta_0 - \beta_\nu) = \frac{\nu(\nu+2)\pi}{3L_\pi}. \tag{3. 9}$$

$$L_\pi = \frac{\pi}{(\beta_0 - \beta_\nu)} = \frac{4n_r W_e^2}{3\lambda_0} \tag{3. 10}$$

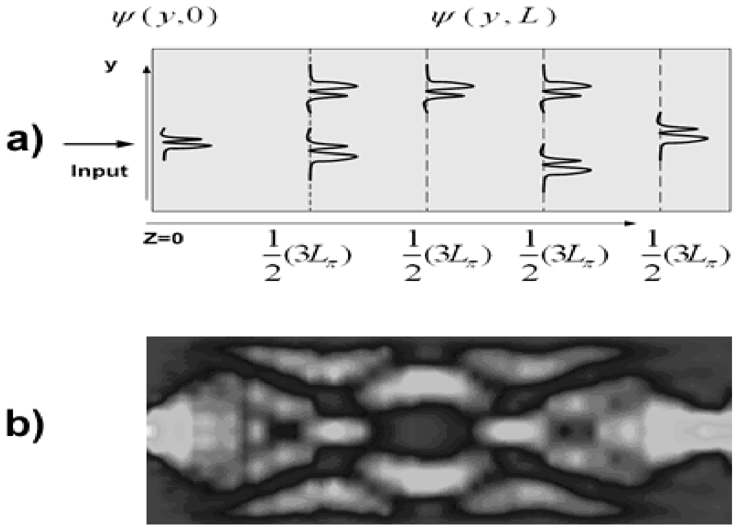

Figure 3. 5: a)Multi-mode waveguide showing the input field, mirrored single image, a direct single image, and two fold images. b)BPM simulation of multi-mode waveguide to illustrate the image formation.

Taking the fundamental mode as a common factor out of the sum, the field profile becomes

$$\Psi(y, z) = \sum c_\nu \psi_\nu(y) \exp[j(\beta_0 - \beta_\nu)z]. \tag{3. 11}$$

Figure 3. 6 shows a step index multi mode waveguide of width W_e and refractive index n_r. It will be seen that under certain circumstances $\Psi(y, L)$ will be a self imaging of input field $\Psi(y, 0)$ with an analytical relation of

$$\Psi(y, L) = \sum c_\nu \psi_\nu(y) \exp[j(\frac{\nu(\nu+2)\pi}{3L_\pi})L]. \tag{3. 12}$$

It can be shown that

$$\exp j\frac{\nu(\nu+2)\pi L}{3L_\pi} = 1 \tag{3. 13}$$

Ł $= p(3L_\pi)$ with $p = 0, 1, 2, ...$ $\Psi(y, L)$ will be the single image of $\Psi(y, 0)$

$$\Psi(y, p(3L_\pi)) = \sum c_\nu \psi_\nu(y) = \Psi(y, 0) \tag{3. 14}$$

and

L = $(\frac{p}{2})(3L_{\pi})$ with $p = 1, 3, 5, ...$ $\Psi(y, L)$ will be the multiple image of $\Psi(y, 0)$

$$\Psi(y, (\frac{p}{2})(3L_{\pi})) = (\frac{1 + (-j)^p}{2})\Psi(y, 0) + (\frac{1 - (-j)^p}{2})\Psi(-y, 0) \qquad (3.\ 15)$$

Similarly, the length at which multiple images form can be determined to be between the direct and mirrored image lengths. The N fold images are formed at

$$L = \frac{p}{N}(3L_{\pi}) \qquad (3.\ 16)$$

Other results appear when restrictions on excitation of the modes come into picture. Restricted excitation allows to design even smaller devices but also has lower tolerances to fabrication parameter variances. In this case, this restricted interference is of two types: paired and symmetric interference. In paired interference, there is selective excitation. If the input beams are launched at symmetric input channels at y=$\pm W_e/6$, the overlap integral will vanish for antisymmetric modes. Therefore c_{ν}=0 for ν=2,5,8,... When the selective excitation is fulfilled the modes contributing to imaging are paired, i.e. the mode pairs 0-1, 3-4, 6-7, ... have similar relative properties, for example each even mode leads its odd partner by a phase difference of $\pi/2$ at z=L$\pi/2$. This mechanism is therefore called paired interference. In symmetric interference case, upon which only 1xN MMI splitters can be designed, only even modes are excited.

$$mod_4[\nu(\nu + 2)] = 0 \quad for\ \nu\ even \qquad (3.\ 17)$$

It is clear that the length periodicity of the mode phase is reduced four times if

$$c_{\nu} = 0 \quad for 1, 3, 5, ... \qquad (3.\ 18)$$

This condition can be achieved by center-feeding the multi mode waveguide with symmetric field profile. The imaging is obtained by linear combinations of the even symmetric modes and the mechanism is called symmetric interference. N fold imaging occurs at even shorter distances, formulated with

$$L = \frac{p}{N}(\frac{3}{4}L_{\pi}). \qquad (3.\ 19)$$

The length of the MMI coupler depends on the width of the multimode waveguide. First of all, it is required to determine the distance between the input ports for sufficient optical insulation between them. Taking this into account, the width the MMI is determined and finally the length of the coupler is calculated from Equation 3. 19. The design is finally confirmed by BPM code.

3.3 Multi-Mode Interference Modulator

Intensity modulation of guided light is one of the most elementary operation in integrated optics. Intensity modulation can be divided into distinct classes such as absorption, radiation and interference based intensity modulation. Example of interference based modulators is Mach-Zehnder interferometers [22]. Mach-Zehnder interferometer (MZI) has been extensively used in realization of optical processing, because of the small device dimensions, excellent tolerance to polarization and wavelength variations, acceptable fabrication tolerance, low excess losses and ability to split light into any number of ports offer superior performance for optoelectronic applications. Figure 3. 6 illustrates the basic structure of an MMI modulator where the input signal is split by a 3-dB MMI coupler and fed into phase shifters and is recombined by another MMI coupler. A MMI based Mach-Zehnder interferometer is limited by power imbalance that may be present at the output of the splitter stage and the output combiner stage. Because of the good balancing MMI based modulators are ideal building blocks for Mach-Zehnder structures [25].

The MZI configuration allows one to change light intensity in the output channel by introducing a phase difference between the two input arms of the second MMI. In the thermo-optic devices, this phase difference is achieved by heating one arm, resulting in a temperature difference between the arms. At the output port, the images of incoming waves interfere. If E_1 and E_2 are the electric field profiles of the incoming waves with ϕ phase shift between them

$$E_1 = \frac{E_0}{2}\cos(wt) \tag{3. 20}$$

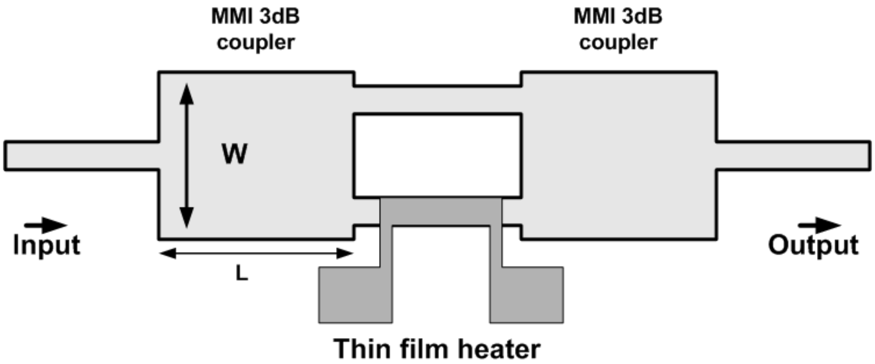

Figure 3. 6: Schematic diagram of MMI modulator.

$$E_2 = \frac{E_0}{2}\cos(wt + \phi) \tag{3. 21}$$

at output port as a result of the interference of two images of incoming waves, we can write the new electric field and power as

$$E_T = \frac{E_0}{2}\cos(wt + \phi) + \frac{E_0}{2}\cos(wt) \tag{3. 22}$$

$$I = \langle E_T^2 \rangle = E_0^2\cos^2(\frac{\phi}{2}) = I_0^2\cos^2(\frac{\phi}{2}). \tag{3. 23}$$

The phase shift can be written in terms of index difference and finally, it is possible to calculate the output intensity as a function of temperature difference

$$I = \cos^2(\frac{\Delta\phi}{2})) = \cos^2(\frac{\pi\chi\Delta T L_h}{\lambda}) \tag{3. 24}$$

where ΔT is the temperature difference between the two waveguide cores of the phase shifter arms, χ is thermo-optic coefficient of the core material, λ is the free space wavelength, and L_h represents the length of the heater. For our devices on Si L_h=1mm, $\lambda = 1.55\mu m$ and χ of $2\times10^{-4}/^0$C, a phase difference of π is achieved with a temperature difference ΔT=3.75 ^{0}C.

Several analytical analysis methods of the MMI coupler based modulators are available [27]. After designing the MMI couplers and cascading them to form the Mach-Zehnder interferometer, we have made use of a mode propagation method

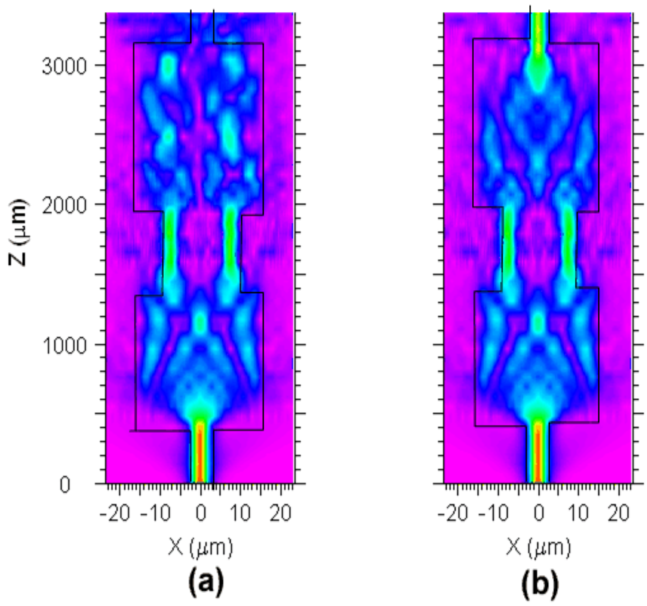

Figure 3. 7: BPM simulation of MMI modulator for off (a) and on state (b).

(BPM) based on effective index (2D) approximation to fine tune the dimensions and confirm the operation of MMI based Mach-Zehnder switch as was explained in reference [21]. Figure 3. 7a shows the BPM simulation of field distribution on MMI modulator where there is a π phase shift between two arms in MZI section and output light intensity is zero and in figure 3. 7b there is no phase shift, intensity of the output light is maximum.

Device Design

We have chosen Bond and Etch Back (BESOI) material with SiO_2 layer thickness $1\mu m$ to create a sufficient optical insulation between the core silicon and the silicon substrate. A schematic illustration of the MMI based MZ modulator is shown in Figure 3. 8. The trench between the waveguides prevents the heat cross flow to create high temperature difference between the phase shifter arms at lower electrical power. The SiO_2 buffer layer between the optical waveguides and evaporated Al heater on the top are required to prevent optical loss. The length of the heater is 1 mm. The distance between single mode waveguides is

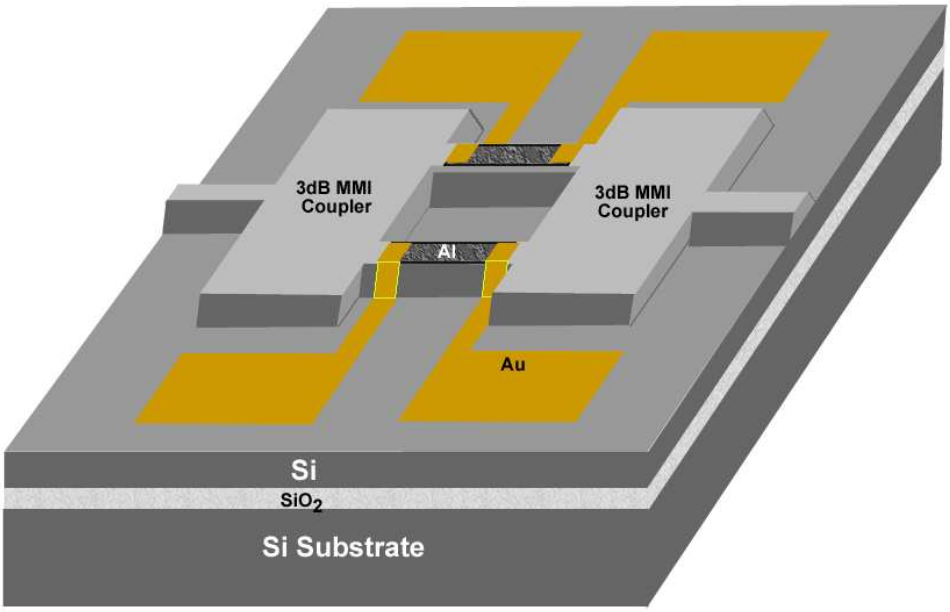

Figure 3. 8: Sidewiev of MMI modulator

chosen as, $12\mu m$ for sufficient optical and thermal insulation. Width of the MMI is chosen as $30\mu m$. Then length of MMI coupler is calculated to be L, $1100\mu m$, using Equation 3. 19.

In order to increase the modulation depth of the switch, single mode condition is required in phase shifter region to prevent different phase accumulation for different modes under the same index change. The exact mode analysis of SOI waveguide is a bit cumbersome and exact analytical solution is difficult to find. Instead we use the approximations described in Section 2.1, namely beam propagation method (BPM) and effective index method (EIM). After an initial design using the EIM, the results were verified with BPM. Single mode condition for SOI waveguides was calculated by making use of the effective index method, the results of which are generalized and plotted in Figure3. 9. Once the top Si layer thickness acting as the core is selected, the area under the corresponding curve in Fig 3.9 define the single mode region and the remaining areas are multi-mode. Thus, it is possible to choose a variety of combinations for waveguide width, w, and the etch depth needed to obtain the required rib height. The

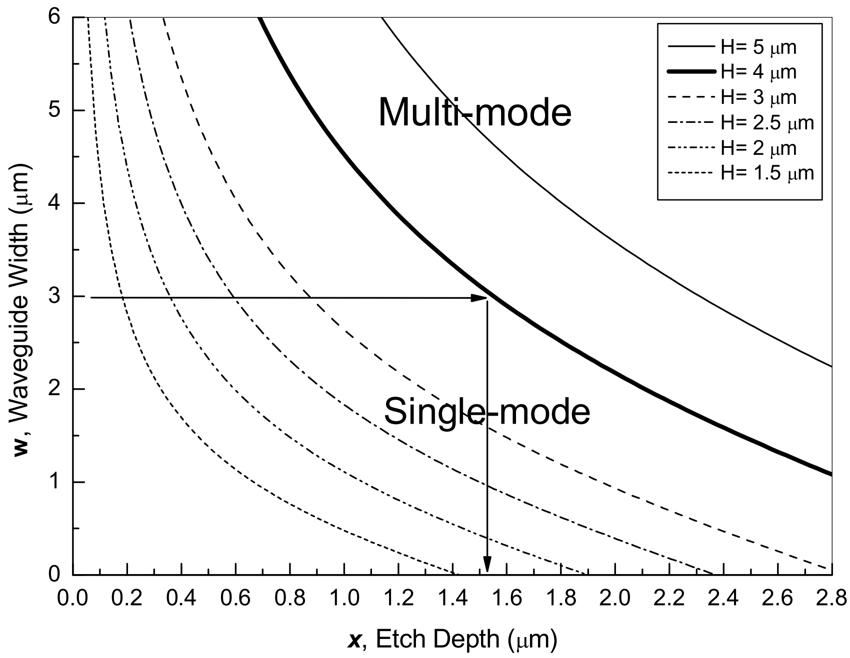

Figure 3. 9: Single mode condition for different Si top layer thicknesses. For H=4 um, waveguide width of 3 um requires the etch depth to obtain the rib as 1.4 um

mode spectrum and shape of the waveguide were both verified by using BPM which solves the scalar or vector wave equation for any structure defined by n=n(x,y,z). The cross section of the single mode waveguide and the mode shape of the TE fundamental mode as obtained by BPM are depicted in Figure 3. 10. Based on these results, a structure for A single mode SOI waveguide was determined with the following parameters; Bottom cladding thickness t_{bc}=1 μm, upper cladding thickness $t_{uc} = 0.2\mu m$, slab waveguide thickness $h_{slab} = 2.6\mu m$, rib height $h_{rib} = 1.4\mu m$ and rib width $w_{rib} = 3\mu m$.

In order to understand the working principles of the thermo-optic switch, a thermal analysis of the device was performed using Finite Element Method (FEM). By doing the thermal analysis, switching power calculation and frequency response of MMI based Mach-Zehnder modulator was obtained using FEMLAB

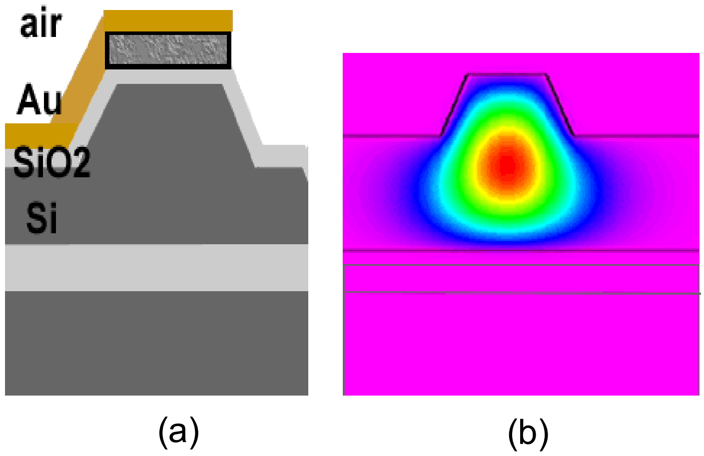

Figure 3. 10: (a)Schematic diagram of waveguide structure, (b) TE fundamental mode shape for Si ridge waveguide as calculated by BPM.

software. FEM was used to perform both linear stationary and time dependent thermal analysis of MMI based Mach-Zehnder modulator. Heat transfer involved in these devices is governed by the heat equation

$$\rho C\frac{\partial T}{\partial t} - \nabla.(k\nabla T) = Q \tag{3. 25}$$

where ρ is the density, C is the heat capacity, k is the isotropic thermal conductivity and Q is the external heat input. In our simulations Q is the heat input provided by the metal heater. We define heat input as heat per unit volume ($W/\mu m^3$) and in time dependent simulations we apply a square wave heat pulse to the metal electrode and calculate the temperature response. The material properties used in all the simulations for Si and SiO_2 can be listed as $\rho_{Si} = 2330kg/m^3, C_{Si} = 703J/kgK, k_{Si} = 163W/mK$ $\rho_{SiO_2} = 2220kg/m^3, C_{SiO_2} = 745J/kgK, k_{SiO_2} = 1.38W/mK$ [32].

Figure 3. 11 shows the simulated two dimensional steady state temperature distribution at the phase shifter region of the MZI. The heater is placed on the left single mode waveguide separated by a trench from the parallel single mode waveguide on the right without a heater. It is observed from the figure, that the power created at the metal heater results in the heat flow into the silicon layer. Surprisingly, the air above the electrodes also heat up but due to the low thermal

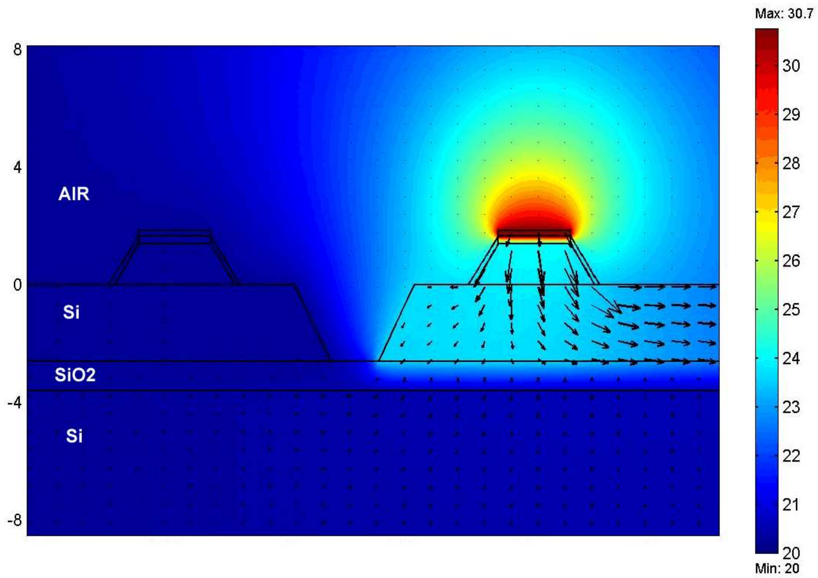

Figure 3. 11: 2D steady state temperature distribution of the MMI modulator. The power applied to the electrode is 114 mW,

conductivity of air, temperature increase is small and consumes only negligible heating power. Temperature distribution at guiding area is uniform. The trench between waveguide arms prevents the heat flow to the alternate waveguide to the left and so creates sufficient temperature difference between them. SiO_2 layer underneath the core layer also effects the heat diffusion, and because of its low thermal conductivity heat diffuses laterally in the silicon layer away from the device rather than into the silicon substrate.

In this simulation, we keep the bottom layer at constant temperature (T=20 ^{0}C) and zero heat inward flux is assumed at the side walls as boundary conditions. From Equation 3. 24, the temperature difference for zero optical output intensity is calculated to be ΔT=3.75 ^{0}C. This is consistent with the simulations using FEMLAB. The trench between the two phase shifter waveguides provides thermal insulation and prevents heating of the parallel second waveguide, allowing for lower switching power and faster response. To obtain the switching power using FEM simulations, we calculated the required heat input from the thin metal film electrode with appropriate boundary conditions. Total switching power P_π was

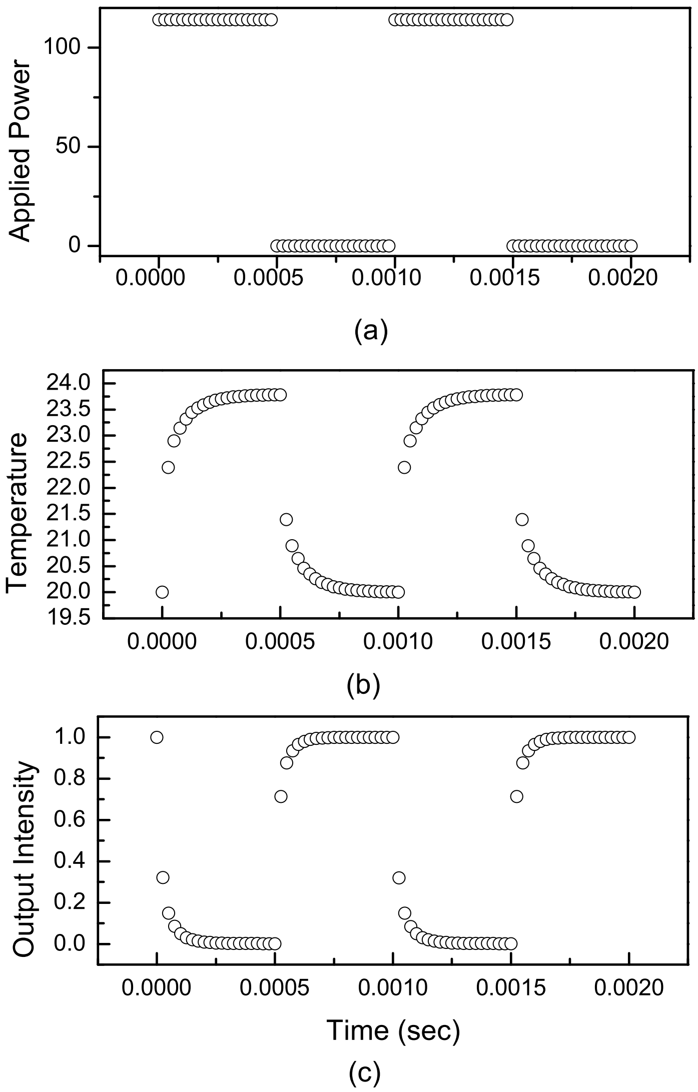

Figure 3. 12: Simulation results of pulse response when 1 kHz square wave is applied to electrode. (a)applied power (b)temperature response (c)output light intensity.

calculated to be 114 mW.

Transient response of the device can also be simulated using FEMLAB software. In this simulation, thermal response and the ensuing optical response of the device to an applied electrical square pulse is calculated. The rise and

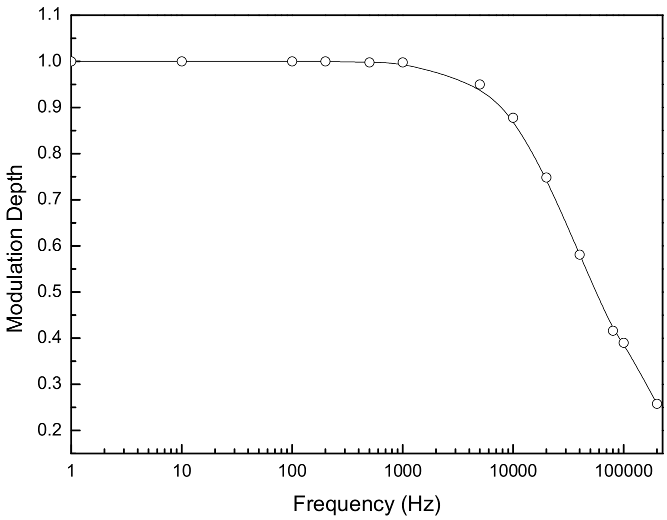

Figure 3. 13: Simulation result for modulation depth of output light intensity as a function of frequency.

falls times of the optical pulses at the output of the device may be limited by thermal and electrical considerations. The amplitude modulation of thermo-optic devices is restricted by thermal rise and fall times. Rise and fall times depend on the thermal properties of the material as discussed in Chapter 2. Heat capacity C and thermal conductivity k determine the temperature rise and fall time. In Fig 3.12, we observe the applied electrical power 114 mW at 1 kHz, the corresponding temperature rise in the waveguide core and the resulting optical intensity response at the output port. It should be noted that the temperature rise upon the application of the electrical pulse is very fast but the temperature fall upon the termination of the electrical pulse is slow and follows an exponential like decrease. This indicates that the frequency response of the devices are limited at the cooling stage as opposed to the heating stage. This is due to the relatively thick SiO_2 layer used under the core layer to optically isolate the core layer. It should be noted that SiO_2 thickness greater than 0.25 μm is sufficient for optical isolation and may decrease the cooling time further. Many simulations at different frequencies were made. A summary of these simulations are plotted in Figure 3. 13. As the frequency of the applied electrical pulse is increased the

Silane (2% SiH_4) Flow Rate)	180 sccm
NH_3 Flow Rate	45 sccm
Process Pressure	1000 mTorr
RF Power	10W
Substrate Temperature	250 ^{0}C

Table 3.1: PECVD process parameters for Si_3N_4 growth.

required temperature difference between waveguides cannot be achieved because waveguide cannot be cooled as fast as the applied electrical power. Therefore, the modulation depth of the output intensity will decrease. The 3-dB cutoff frequency can be observed from figure 3. 13. Modulation depth is within 50% of its maximum value at 50 kHz when a the switching power of 114 mW is applied.

Device Fabrication

We start the fabrication process by cleaving a SOI chip with dimensions of 10×20 mm^2 from the wafer. SOI based waveguide devices are typically formed on the top silicon layer. In order to etch the silicon, pattern transfer is done by using specific solutions resulting in etching of the uncoated regions. Potassium hydroxide (KOH) solution is one of the anisotropic wet etchants of Si [30]. In conventional lithography process UV light sensitive photoresist (PR) is used for pattern transfer. However, PR cannot withstand to KOH solution and as such PR cannot be used as a mask to etch Si. So silicon nitride (Si_3N_4) film is required to use as a hard mask for pattern transfer. For this purpose the chip is degreased in a three solvent cleaning process prior to covering its top surface with a layer of Si_3N_4. After sample cleaning and drying the chip at 120 ^{0}C for 60 sec , the sample is coated with Si_3N_4 by plasma enhanced chemical vapor deposition (PECVD) technique. A fully automated planar plasma reactor have been used (Plasmalab 8510C). The growth rate depends on the process parameters. The recipe file which results in a growth rate of 100 A^0 /min Si_3N_4 is given in Table 3.1.

The cleaned sample is placed on the lower electrode plate of the PECVD unit which is heated before the process starts. After 2000 $A^0 of$ Si_3N_4 deposition, the

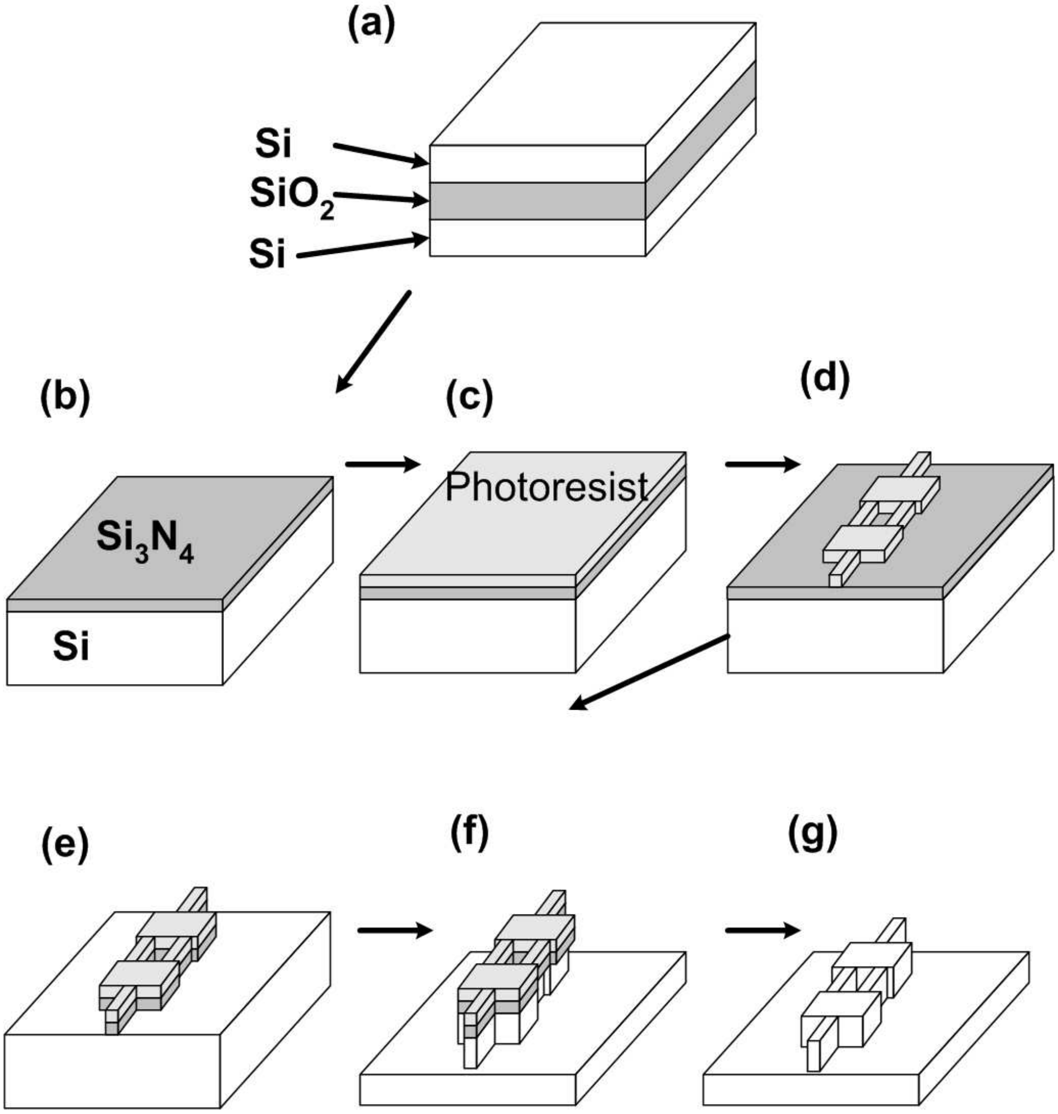

Figure 3. 14: All Patterning steps of SOI optical waveguides, (a)SOI structure, (b)Si_3N_4 Deposition, (c)Photoresist Spinning, (d)Photolithography, (e)HF Etching, (f)KOH Etching, (g)Removing Si_3N_4

pattern transfer is accomplished by conventional optical lithography. Surface of the sample is coated with AZ5214 photoresist by spinning at 5000 rpm for 40 sec. The uniformly PR coated sample is dried on a hot plate at 120 ^{0}C for 50 seconds so as to evaporate the polymer solvent of the PR and to polymerize the PR.

This results in a layer of photoresist with thickness of 1.4 μm. Then the mask is aligned in the mask aligner (Karl Suss MJB-3 HB/200W). After exposing with UV lamp, the sample is developed in AZ400K developer solution to remove the exposed material. PR pattern is transferred to the $\mathrm{Si_3N_4}$ layer. by etching Si_3N_4 in a dilute HF solution. In this process PR behaves as the masking material. In order to increase the hardness of PR baking at 120^0C is used before etching in dilute HF solution. The HF solution is a mixture of 1:1000 HF:$\mathrm{H_2O}$ and has a etch rate of 34 A/s. The PR is then removed by acetone (ACE). Finally, the sample is ready for etching in a KOH solution using Si_3N_4 as the etch mask.

It is important to note that for low loss waveguides minimum surface roughness of the waveguide walls is required. Due to the anisotropic etching properties of KOH solution, KOH solution parameters such as concentration and temperature need to be optimized. As a result, a solution of 1:3:1, KOH:H_2O:ISO at 40 ^{0}C is chosen as optimum parameters. The etch rate of this solution is 470 ^{0}A/min. The etch depth for a single mode rib waveguide requires that the silicon layer be etched approximately 1.4μm. Therefore, etching the ribs with KOH solution takes 30 minutes. After KOH etching, the Si_3N_4 mask is removed by the same HF solution used earlier. Figure 3. 14 illustrates the fabrication steps for waveguide patterning. After the etching the waveguide pattern, second step is to define the trench between the waveguides. Trench is etched in silicon with standard optical lithography process used earlier. Si_3N_4 is used as a hard mask again. First, the sample is coated with Si_3N_4 and then using PR and conventional photolithography the trench pattern is transferred to the PR. The second step is to transfer the PR pattern onto Si_3N_4 layer by using dilute HF. Figure 3. 15 illustrates the trench patterning steps. Then PR is removed and then using KOH solution, trench is etched in silicon. Finally, Si_3N_4 mask is removed with dilute HF solution. Care must be taken at this step to assure best alignment possible of the trench with the waveguides, since the device is relatively long.

The next fabrication step is PECVD $\mathrm{SiO_2}$ deposition for top cladding layer. There are three requirements for this deposition: Firstly, the thickness of the layer should be large enough for optical insulation between guided light and metal

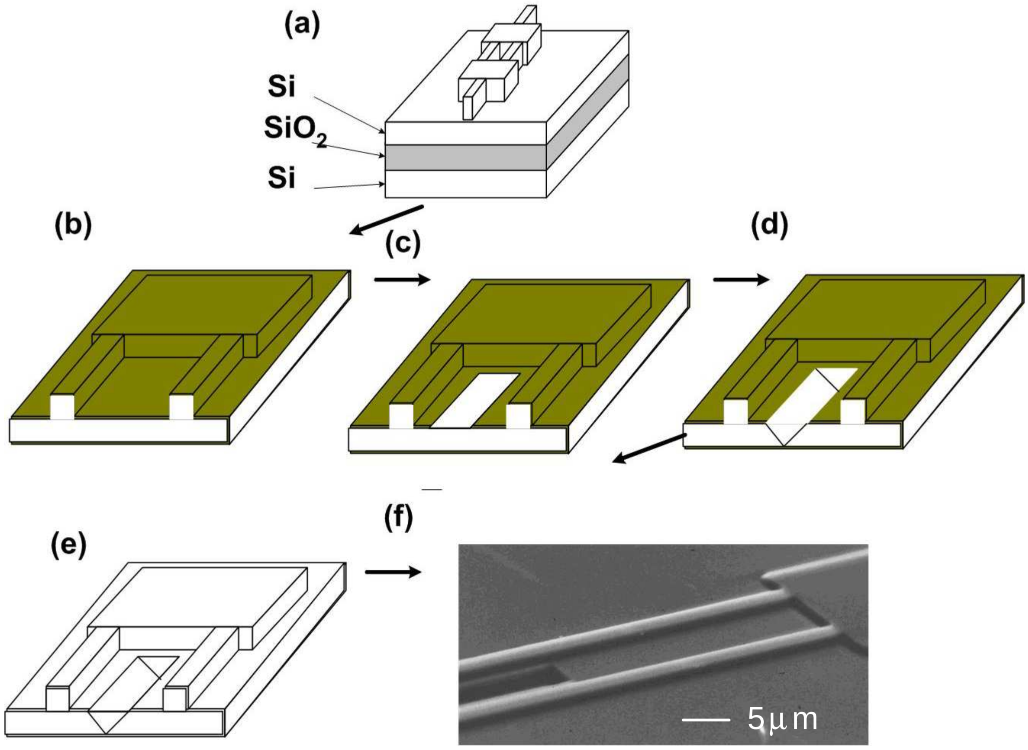

Figure 3. 15: Trench patterning steps of SOI optical waveguides (a) Si MMI waveguide, (b) Si_3N_4 Deposition, (c) Defining trench pattern, (d) KOH Etching, (e) Removing Si_3N_4, (f) SEM photograph of MMI modulator .

Silane (2% SiH_4) Flow Rate)	180 sccm
N_2O Flow Rate	25 sccm
Process Pressure	1000 mTorr
RF Power	10W
Temperature	250 ^{0}C

Table 3.2: Process Parameters for SiO_2.

heater. On the contrary, the second requirement is that the SiO_2 be thin for good heat transfer. By using BPM simulation the calculated minimum thickness for optical isolation is found to be 0.25 μm. Finally, the optical quality of the oxide layer should be sufficient for minimizing the optical loss. SiO_2 is grown by PECVD with the process parameters listed in table 3.2. This recipe results in a layer of SiO_2 with refractive index of 1.473.

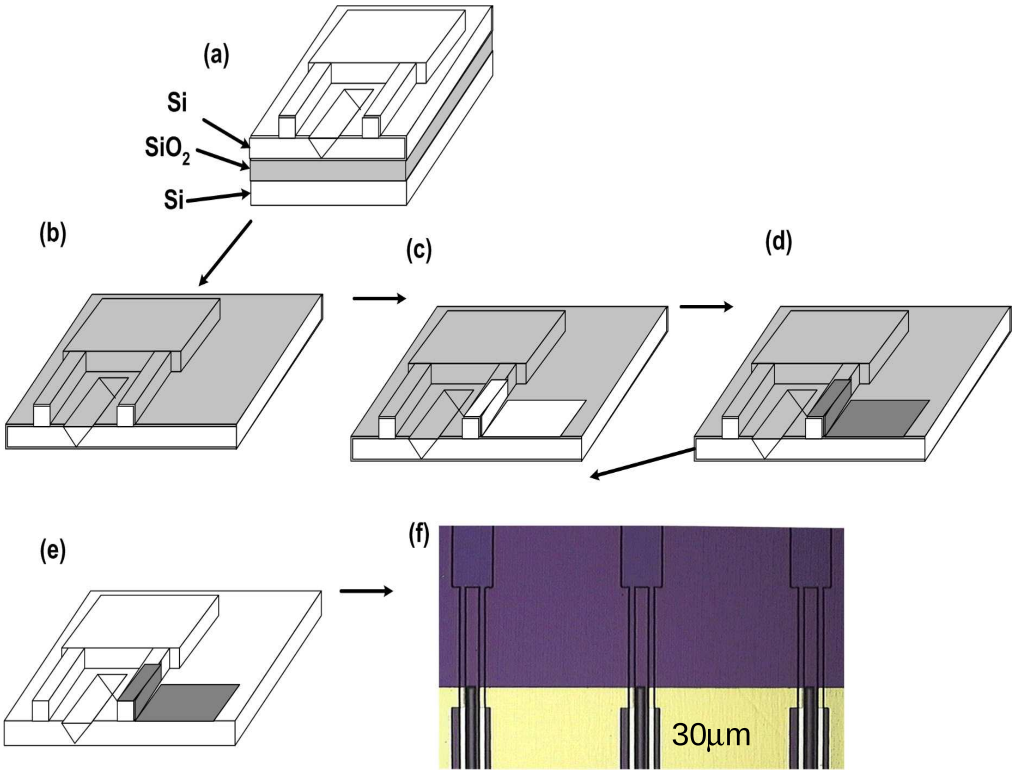

Figure 3. 16: Electrode metallization of thin film heaters (a) Patterned Si waveguide, (b) Spinning PR, (c) Defining heater, (d) Al evaporation, (e) Liftoff, (f) Top view optical microscope photograph of heaters and electrodes.

The final step is patterning the metal heater. The thin film electrodes were formed by conventional lift-off process. Aluminum is suitable material as a metal heater because of its adhesive properties on SiO_2 surface and its low electrical resistance. First, electrode patterns were defined by photoresist and then Al was evaporated on the sample. Then, by rinsing in ACE the photoresist and the Al on it was removed. Figure 3. 16 illustrates this process. The thickness of the Al film is very important parameter in order to reach acceptable heater resistance. Evaporation is more suitable for low resistive metal deposition. Grain formation in metal film during sputtering increases the resistance dramatically. For a heater with a resistance of 50 Ω we deposited $0.2\mu m$ thick 1 mm long and 3 μm wide Al electrode using standard thermal evaporation process. Final devices require that waveguide facets be of very good quality. This can be obtained with a cleaving process. It was found that thinner substrates produce better facets upon cleaving. Therefore, finished devices were covered with PR and glued on a Si wafer for back side etching. A KOH solution at 50 ^{0}C for 40 hours is used to thin down the substrate to approximately 200 um. After cleaning the device, a Si cleaving pen is applied from the back side to cleave the devices at the desired location.

Results

Figure 3. 17 shows our optical measurement setup. 1.55μm DFB laser (LDM-7980) is coupled to cleaved facets with a single mode fiber. In this setup, light is coupled into the waveguide by bringing the fiber carrying the light in close proximity to the waveguide facet. This butt-coupling technique requires optically cleaved facets for the devices. For TE and TM measurement polarization of the laser was controlled via a polarization controller and checked by a polarizer at the output. A field microscope is used to align the fiber with the end facets of the waveguide. The light exiting the device may be collected by a microscope objective or by another single mode fiber, both of which are available on the setup. The light is then detected either by a photodiode detector or by an IR camera (Electrophysics Microviewer 7290A) with the help of a focusing lens. Both Ge and InGaAs photodiodes (Thorlabs DET410) have been used. The photodiode output is monitored by powermeter for d.c. measurements or by an oscilloscope (HP 54603B) for a.c. measurements. The DFB laser used in this work lases at 1.55 μm which can be tuned by controlling the temperature of the device. For modulation purposes, external electrical signals are applied by using probes with fine tips touching the aluminum pads on the devices. The probes are fed by a signal generator (HP 8116A) that can provide square wave pulses up to 50 MHz with amplitudes of up to 15 V.

Figure 3. 18 shows the fundamental TE mode of the MMI Modulator in the ON state as seen on the IR camera. TM mode behaves similarly after maximizing the output light intensity by fine tuning fiber position at the input waveguide and collection optics with the help of the IR camera, collected signal is routed onto the photodiode. Since the devices were designed to be normally ON, it was not

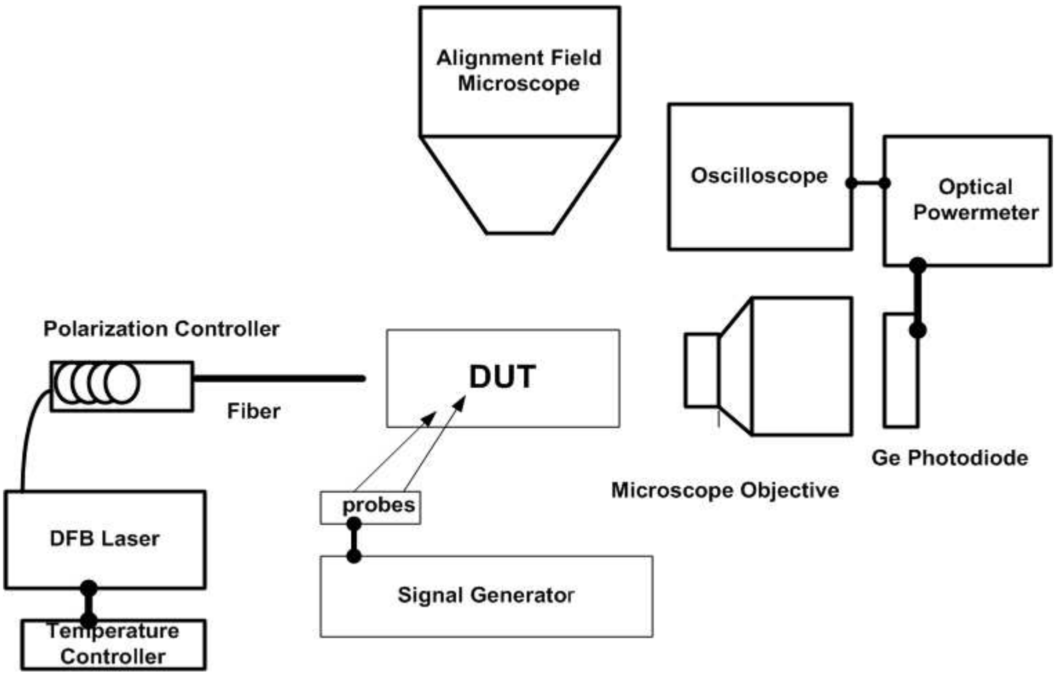

Figure 3. 17: Optical measurement setup.

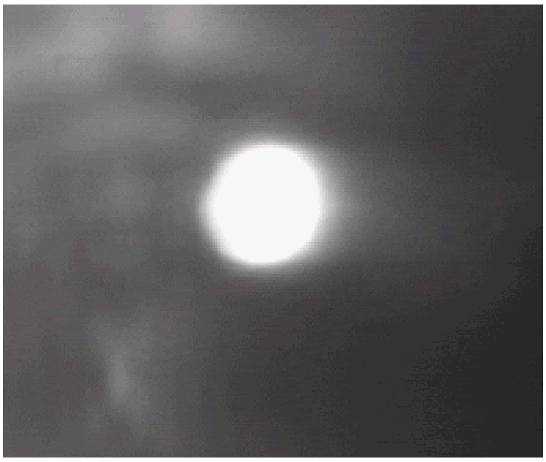

Figure 3. 18: View of TE_0 mode as captured with IR camera.

difficult to find the output light. At this point insertion loss of the devices were measured. Insertion loss includes all the losses that occur when the devices is inserted between the fiber and the collection optics and includes coupling losses due to differing fiber size and waveguide cross section, propagation loss through

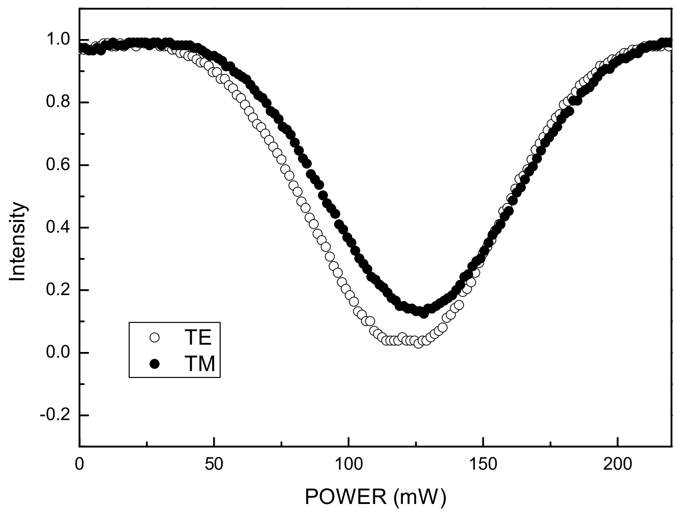

Figure 3. 19: Normalized output light intensity as function of applied electrical power.

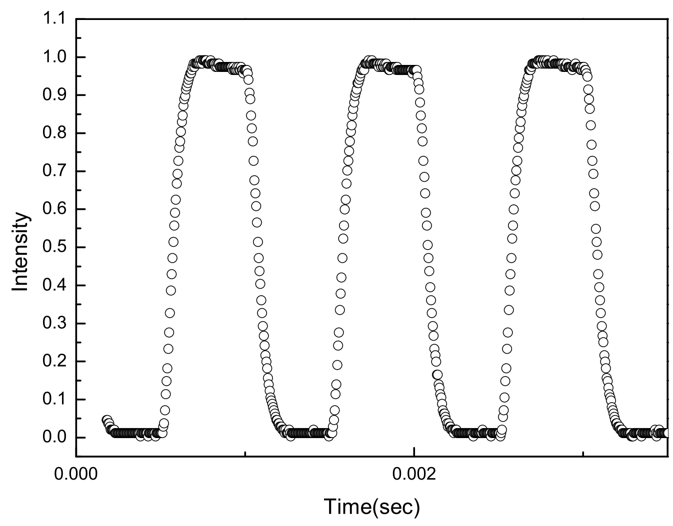

Figure 3. 20: Measured normalized pulse response when a square-wave voltage pulse with a 1KHz was applied.

the device, and Fresnel reflection at the input and output facets. The fiber core size of the single mode fibers is 9 μm in diameter, it is expected that there will be a large coupling loss for these devices. Furthermore, propagation losses for MMI based devices are known to be relatively large and modulation of the light output further increases this. Finally, Fresnel reflection is due to inherent reflection coefficient of the Si facets and may be considered to be relatively large compared to fibers related loss due to large index contrast of the waveguides under measurement. The insertion losses may be reduced by using the well known techniques of appropriate tapering at the input and output of the devices, and by antireflection coating the waveguide facets.

To determine the turn off power (P_π), the ramp voltage was applied to one of the heater and output intensity was recorded for both TE and TM polarizations. According to Figure 3. 19 the measured switching power is approximately 120 mW for both TE and TM. As seen from the Figure 3. 19 output light intensity is minimum when 120 mW power is applied. This result agrees well with our calculated power P_π with FEM simulations which was found to be 114 mW. We suspect that 6 mW power difference between the calculated and the observed values stems from the longitudinal heat diffusion. To reduce computing time and satisfy stringent memory requirements, our simulations were done in two dimensions which cannot account for longitudinal heat loss along the waveguide.

For time dependent response measurements a square wave voltage signal was applied to the heater. Figure 3. 20.b shows the modulated output signal, where 1 kHz signal was applied 3. 20.a. This measurement was repeated for many frequencies the results of which are plotted in Figure 3. 21. At higher frequencies, due to low thermal rise and fall times, modulation amplitude decreases. Figure 3. 13 shows that for our MMI modulator at 60 kHz the amplitude modulation falls within 50% of its maximum value 3-dB cutoff frequency is 60 kHz. This result also agrees as a representative example, Figure 3. 13 reasonably well with our FEM simulation which is shown in Figure 3. 21. The small difference between simulation and experiment stems from the difference of the material properties used in the simulation.

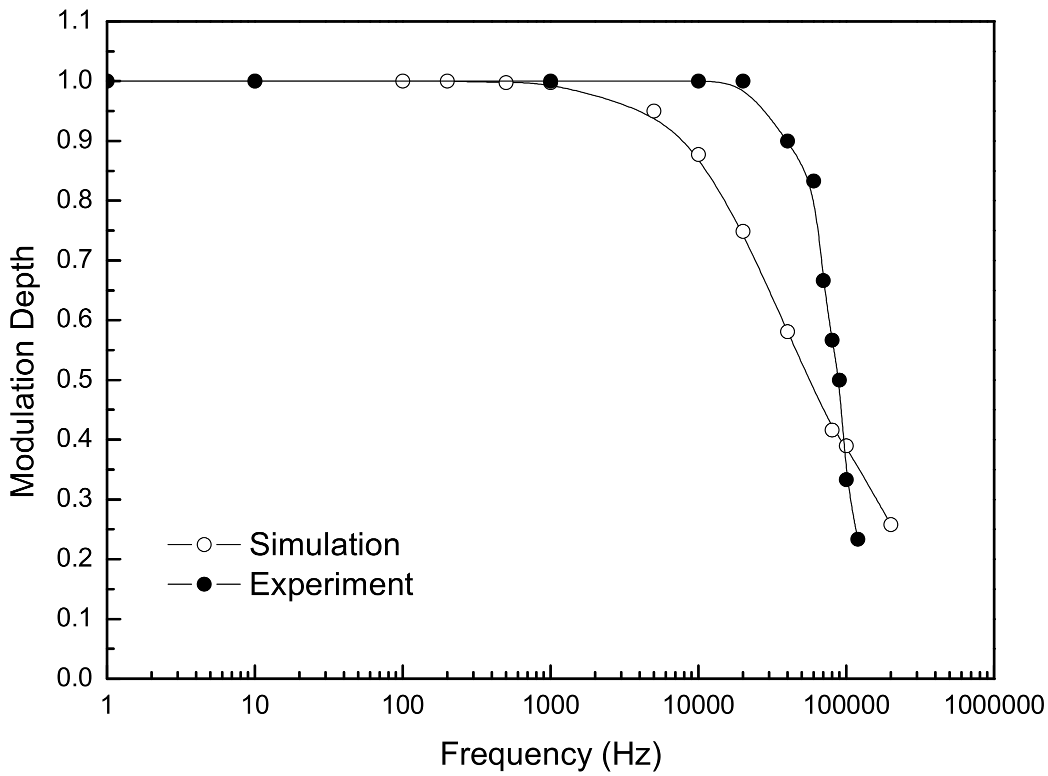

Figure 3. 21: Normalized modulation depth as a function of frequency.

Chapter 4

Thermo-Optic Y-Junction Mach-Zehnder Modulators

In this chapter, Y-junction based Mach-Zehnder interferometer is investigated. Both silicon based and polymer based devices were fabricated and their characteristics measured.

4.1 Y-junction Coupler

Mach-Zehnder interferometer (MZI) is the most commonly used optical device for coherent light modulation [22]. The principle of MZI is to split light into two different paths and then to recombine them at the output port. This splitting and recombination of guided waves can be achieved by different types of couplers such as Y-junction and multi-mode interference couplers. In this chapter, we will discuss the Y-junction 3-dB couplers and Mach-Zehnder modulators based on them. Figure 4. 1 illustrates the basic structure of Y-junction coupler.

Power splitting in Y-junction coupler is achieved by adiabatic transition from a single mode waveguide to two single mode waveguides. Figure 4. 2 represents the adiabatic transition in a Y-junction coupler. The input channel and two output channels of the coupler are all single mode. Incoming wave can only excite the first optical mode in both channels, and field profile is conserved but

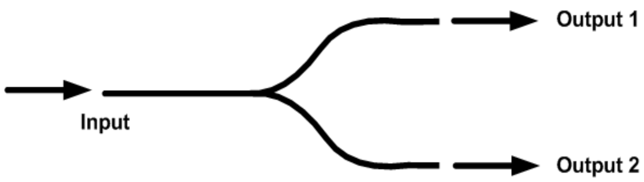

Figure 4. 1: Schematic diagram of MZI coupler.

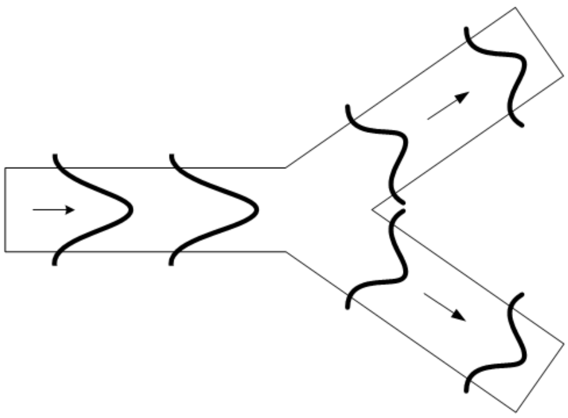

Figure 4. 2: Schematic diagram of adiabatic transition.

the total power is divided to the half of its initial value in the input channel. In addition to balanced division of power between outputs channels low optical loss is also needed. In splitting the incoming optical power into two noninteracting waveguides, the curvature of the outgoing waveguide needs to be above a critical radius, below which significant bending loss can occur [23]. Thus, radius of the Y-branch must be large enough to avoid the optical loss. However, it should be small enough in order to minimize the length of the total device.

4.2 Thermo-Optic MZI Modulator

As shown in Figure 4. 3 the MZI consists of two back to back Y-junction couplers and two single mode waveguides serving as phase shifting regions between the Y-junction couplers, they connect. The input field profile given by

$$E = E_0 \cos(wt) \tag{4. 1}$$

can be decomposed into two first order modes represented by

$$E_1 = \frac{E_0}{2} \cos(wt) \tag{4. 2}$$

$$E_2 = \frac{E_0}{2} \cos(wt) \tag{4. 3}$$

Due to the adiabatic transition adopted in the design of the Y- junction, mode profiles are the same at the output channels. They interfere at the output channel and if the optical path lengths of the guided beams are different because of a phase shift, the intensity will change as a function of the phase shift, given by

$$E_T = \frac{E_0}{2} \cos(wt + \phi) + \frac{E_0}{2} \cos(wt) \tag{4. 4}$$

$$I = \langle E_T^2 \rangle = E_0^2 \cos^2(\frac{\phi}{2}) = I_0^2 \cos^2(\frac{\phi}{2}). \tag{4. 5}$$

The phase shift on the arms of the interferometer may be induced by several means, including the use of strain, temperature induced index change (thermo-optic effect) and electric field induced index change (electro-optic effect). In this work, thermo-optic effect was used. If we write the phase shift in terms of temperature difference between the arms of the interferometer, we can find the output intensity as

$$I = I_0 \cos^2(\frac{\Delta\phi}{2})) = I_0 \cos^2(\frac{\pi\chi\Delta T L_h}{\lambda}). \tag{4. 6}$$

In thermo-optic devices, lower switching power can be obtained by using materials with high thermo-optic coefficients and low thermal conductivity [31]. However, low thermal conductivity restricts the speed of the modulation. We fabricated two different Y-junction MZI modulators. First was a silicon based modulator with high thermal conductivity for high speed modulation, and second one was polymer based, with low thermal conductivity for low power applications.

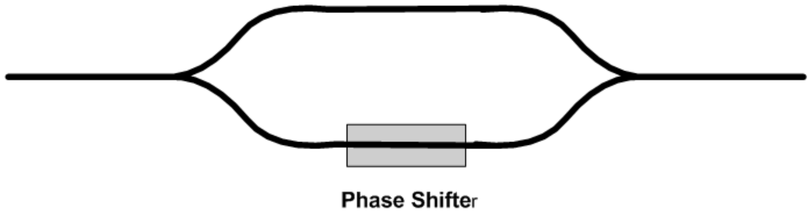

Figure 4. 3: Schematic diagram of MZI modulator.

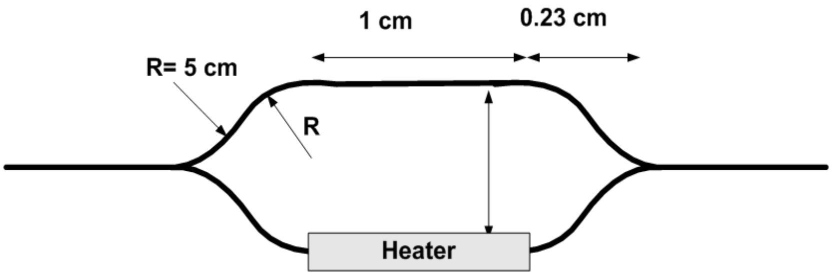

Figure 4. 4: Schematic diagram of MZI structure used in modulator .

4.2.1 Silicon Based Thermo-Optic Modulator

As shown in Figure 4. 4, the Y- junctions were constructed by using portions of a circle with opposing centers, whose radii of curvature were chosen to be 5 cm each to minimize bending loss. The heater length was 1cm. The thermo-optic coefficient of silicon is $2 \times 10^{-4}/^{0}$C and for 1cm heater length, the needed temperature difference to achieve π phase shift is 0.37 ^{0}C. Waveguide structure at single mode condition was defined earlier as depicted in Figure 3. 9.

In order to calculate the expected total power consumption to turn off the device (P_π), FEM simulation has been used. From 2D simulations, the required power was found to be higher than that of MMI based Mach-Zehnder modulators. The power difference between Y-junction based and MMI- based modulators stems from the 2D heat diffusion [32]. In MMI based Mach-Zehnder modulator the trench between waveguides allows heat flow in only one lateral direction. There is no trench in Y-junction modulator between the arms. The heat flow occurs in both lateral directions so that the total power consumption is expected to increase. The calculated P_π power for Y-junction based Mach

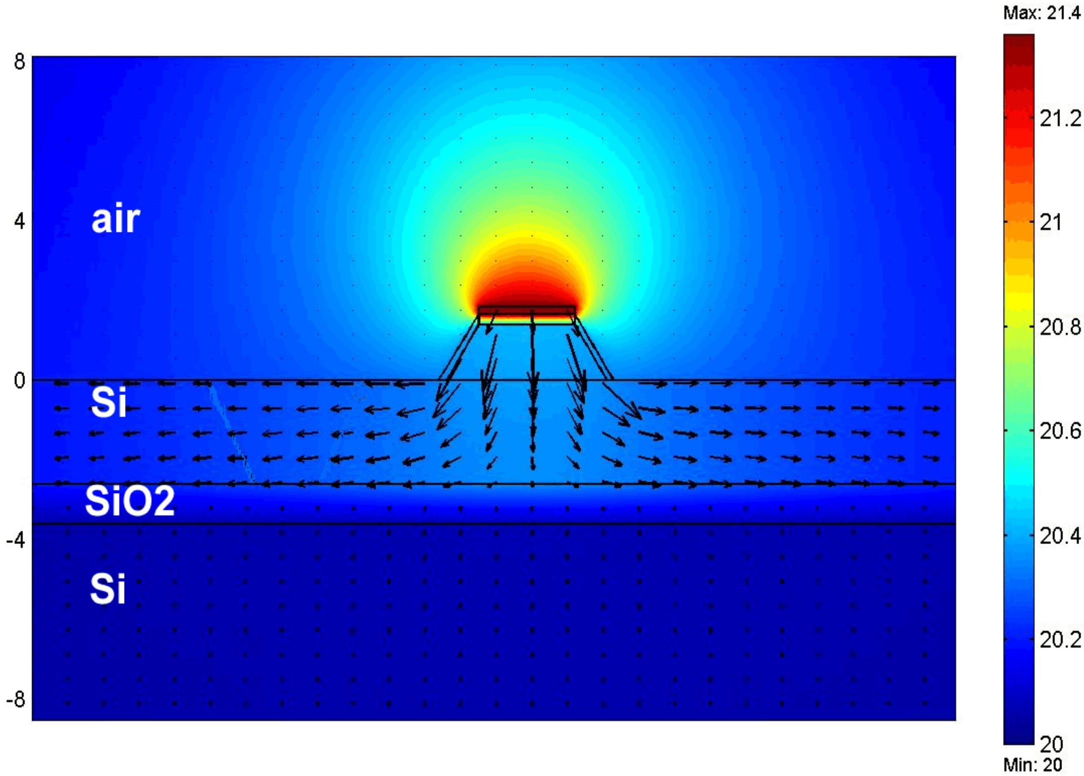

Figure 4. 5: Simulated 2D temperature profile of MZI.

Zehnder modulators, is found to be 162 mW. Figure 4. 5 represents the simulated temperature profile. As shown in Figure 4. 5 heat is created by the metal electrode and flows in to both directions. Power consumed by air is negligible because heat conduction in air is very small due to its low thermal conductivity and mass density. Arrows show the magnitude and direction of the heat flow. Because of the low thermal conductivity of the SiO_2 layer, heat diffuses into silicon layer. Since there is no trench for thermal isolation of the waveguides, power requirement increases. Distance between the two waveguides is large enough so as to prevent the crosstalk between two guiding waveguides. Therefore a temperature difference of 0.37 ^{0}C can be achieved with 162 mW operating power.

From time dependent simulations [33], it is observed that the temperature rise is the same as for MMI based modulator. Figure 4. 6 shows the temperature rise time for Y-junction based Mach-Zehnder modulator. After 10 μsecs, temperature

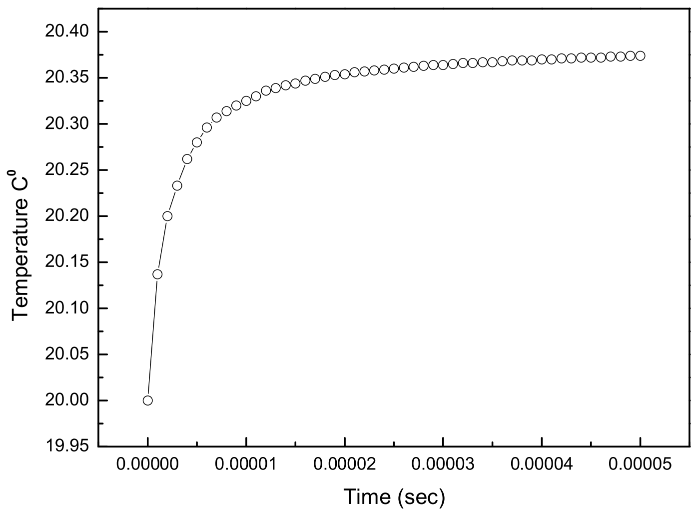

Figure 4. 6: Simulated temperature response for MZI.

reach its saturation value. The saturation temperature is the steady state temperature of that point. The rise time, therefore, is about 10 μsec.

Device Fabrication

Device fabrication of Y-junction based Mach-Zehnder modulator consists mainly of two steps, first step is patterning waveguides and etching them and the next step is preparing heater electrodes and contact pads. The detailed description of Si waveguide fabrication was given in Chapter 2. Briefly, the fabrication steps can be summarized as follows; After degreasing the sample in a three solvent cleaning procedure, samples are coated with PECVD grown Si_3N_4 at 350 ^{0}C. The process parameters used were as shown in Table 3.1. After PECVD deposition, Y-junction based MZI pattern is transformed to photoresist (AZ 5214). By etching the exposed areas of Si_3N_4 in dilute (1:100)HF for 1 min, same pattern is transferred onto Si_3N_4. After removing the photoresist using an acetone bath, a KOH solution is used for Si etching. Finally, Si_3N_4 is removed using the same HF solution used earlier to define the waveguide pattern onto the Si_3N_4. After fabrication of waveguides, SiO_2 deposition is required to isolate the metal heater

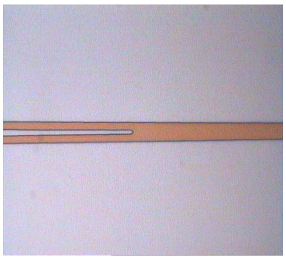

(a) Si_3N_4 mask

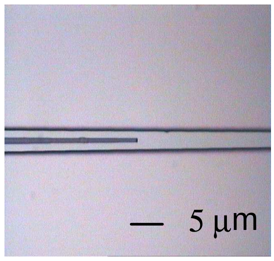

(b) Si waveguide after KOH etching

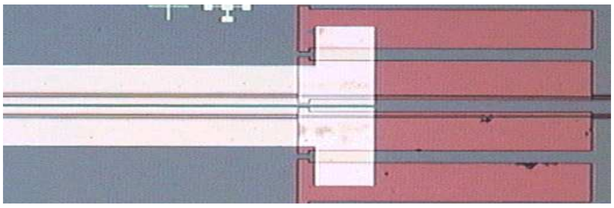

(c) Al heater and electrodes

Figure 4. 7: Fabrication steps for MZI

electrodes to be deposited onto the interferometer arms. A $0.25\mu m$ thick oxide layer was calculated to be enough for optical isolation between the guiding layer and metal electrodes. SiO_2 was deposited using PECVD with the same recipe given in Table 3.2. Finally, Al heater and electrodes were patterned by lift-off process. Details of the lift-off process were described in Chapter 2. Figure 4. 7 represents the fabrication steps. 0.2 μm Al is deposited with thermal evaporation with 10 ^{0}A per sec deposition rate.

4.2.2 Polymer Based Thermo-Optic Modulator

Thermo-optic switches are attractive devices for low speed optical communications. The main goal of the present research [34] is to reduce the operating power. In order to reduce the heating power, a bridge suspended structure has been proposed for silica based devices in the literature [35]. The reduction in heating power by a factor of about 10 is achieved at the price of a considerable increase of switching times from 2 to 50 ms. Changing the basic waveguide material is necessary to optimize the device configuration. In addition to excellent processability and low cost fabrication, their low thermal conductivity make organic polymers good candidates for thermo-optic materials [36]. However, low thermal conductivity during the fabrication process restricts the modulation speed and also low thermal stability is the main drawback for polymer based devices. Glass transition temperature (T_g) determines the operating temperature of the devices because at temperature higher than T_g the viscosity, thermal expansion coefficient and refractive index are change dramatically.

In order to guide an optical wave in a confined structure, refractive index difference is needed, typically supplied by different materials surrounding the core layer. High speed devices need high thermal conductivity, nonetheless for low power application low thermal conductivity is required. However, nearly all polymers suitable for waveguide fabrication have similar thermal properties. To obtain higher modulation speeds, upper and lower cladding materials should be chosen with higher thermal conductivity than the core material. SiO_2 is a good candidate for this application. However, care should be taken to choose proper deposition parameters in the presence of polymer layers. Most polymers are not thermally stable at high temperatures. While it may be possible to deposit SiO_2 by magnetron sputtering at low temperatures, it is well known that layers deposited by magnetron sputtering result in waveguides with high loss. However, using PECVD, low loss SiO_2 layers can be grown at temperatures as low as 250 ^{0}C. Depositing SiO_2 as a top cladding of a polymer core, requires that a thermally stable polymer be chosen as the waveguide core material. Since, high thermal stability is determined by the high glass transition temperature of the polymer we utilized a commercially available and highly temperature stable ($T_g \geq$ 350 ^{0}C)$Cyclotene^{TM}$ with an index of refraction of 1.55. Table 4.1 lists the material properties of the used material. Figure 4. 8 represents the basic device structure and FEM simulation of temperature distribution. As shown in Figure 4. 8 heat diffuses into SiO_2 layer from metal heater and increase the guiding layer temperature. Because of the relatively high thermal conductivity of SiO_2, temperature rise time is lower than polymer cladding based thermo-optic devices. The heat capacity of polymer is higher than silicon so same

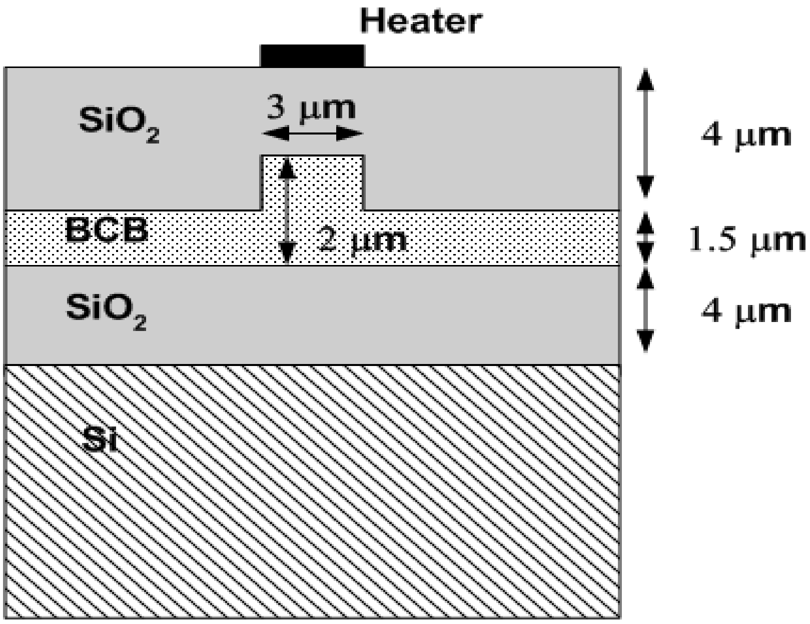

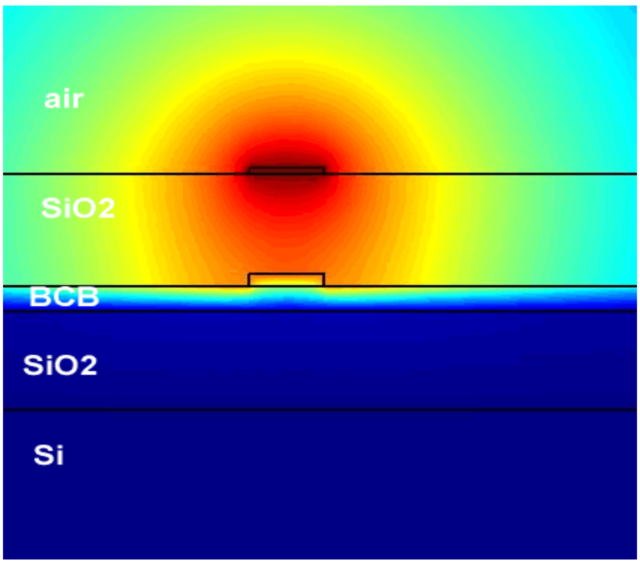

Figure 4. 8: Schematics of polymer device structure and FEM simulation of temperature distribution.

temperature difference can be achieved by consuming the low power. The thermo-optic coefficient of BCB (Bisbenzocyclobutene) is -1$\times10^{-4}/^{0}$C so the required

	ρ(kg/m^3)	C$_p$ (J/kgK)	K (W/mK)	n
BCB	1050	1170	0.2	1.55
Si	2330	703	163	3.48
SiO_2	2220	745	1.38	1.46

Table 4.1: Properties of used waveguide materials.

temperature difference to create π phase shift in 1cm heater region is 0.75 ^{0}C. In FEM simulation 30×10^{11}W/m^3 power source in applied. The resulting total power consumption was 18 mW. The lateral heat splitting also increases the power requirement. By etching trench, this heat diffusion can be decreased and the lower power operation can be achieved.

Refractive Index Measurements of BCB Films

As the preparation methods of polymer films may affect their refractive indices, it is important to measure the refractive index of BCB films to make sure that it is within the tolerance limits of the single mode waveguide. In order to measure the refractive indices of the BCB films prism coupling technique was used. In this technique a slab waveguide was formed by using the film of interest as a core layer, 9.9 μm thick thermally grown SiO_2 layer as a lower cladding and air as the upper cladding. In this method lowest order guided modes can be excited by making use of a prism coupler. A prism coupler setup is shown in Figure 4. 9, where the prism is located at a distance h from the surface. A beam of light is directed into the prism with refractive index n_p such that a total internal reflection occurs at the air-prism interface. The index of refraction of the film is n_{core}, that of the lower cladding SiO_2 layer n_{SiO_2} and for the outer region n_{air} was taken to be equal to one. The condition for total internal reflection is satisfied when [37]

$$\theta_p > sin^{-1}(\frac{n_{air}}{n_p}) \tag{4. 7}$$

This gives rise to standing wave formation inside the prism, the k vector of which is given by

$$\vec{k_0}n_p = n_p(\pm k_x\hat{x} + k_z\hat{z}) \tag{4. 8}$$

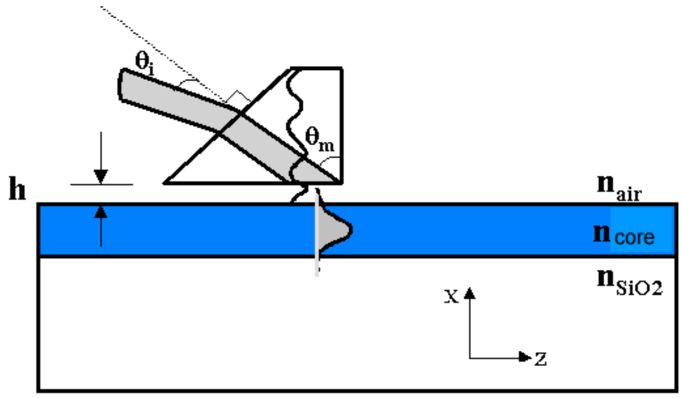

Figure 4. 9: Schematic representation of of a prism coupler setup..

$$= \quad n_p(\pm k_0 cos\theta_p \hat{x} + k_0 sin\theta_p \hat{z})$$

Outside the prism the field decays exponentially, but the z component of the wavevector remains the same. As evident from equation 4. 8, k depends on the angle of incidence θ_p, which may enable us to adjust and possibly match the velocity of propagation of the wave in the prism with that in the guide. The condition of matching of the β terms is given by

$$k_0 n_p sin\theta_p = \beta_f \tag{4. 9}$$

,β_f being the propagation constant in the polymer film. Therefore, at an angle θ_p a coherent coupling of energy is achieved. By changing θ_p it is possible to select the desired mode of excitation. Few important points should be mentioned. First, the most effective coupling occurs when the spacing of the air gap h is at the order of one-fourth of the vacuum optical wavelength, and next, due to the above mentioned conditions the index of refraction of the prism should be greater than that of the film. In our measurements a SF14 crystal with n=1.75606 (λ=632.8 nm) was used for excitation of the waveguide modes. A schematic representation of the prism coupling measurement (PCM) setup which was built in our laboratory is given in Fig. 4. 10.

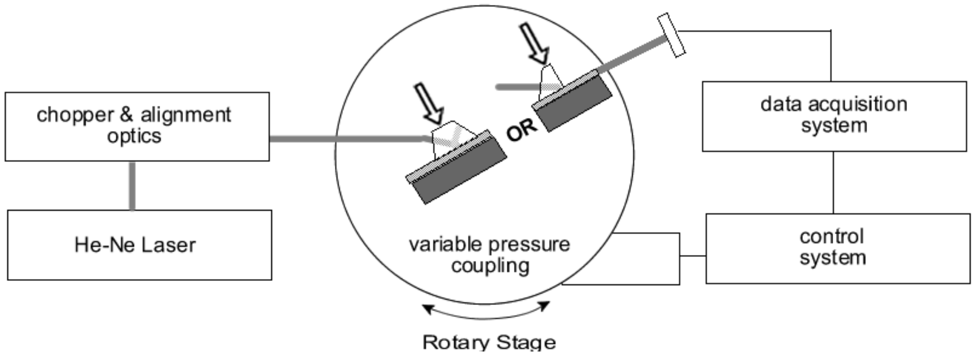

Figure 4. 10: Experimental setup for measuring the coupling angles. The laser beam is incident on the coupling prism. The prism coupler setup is mounted onto a high precision rotary stage with stepper motors with a precision of better that $\pm$ 0.01^o

Alignment optics includes a polarization rotator and an analyzer in addition to a chopper. A beam splitter was also included to calibrate the relative orientation of the laser beam with respect to the coupling prism and was used to establish the origin of the angular displacement. The coupling pressure was adjusted by a micrometer holder in contact with a calibrated spring system that allowed us to monitor the applied force onto the prism. The operational procedure of the PCM is simple. The linearly polarized monochromatic light, of 632.8 nm wavelength from a He-Ne laser, with either transverse electric (TE) or transverse magnetic (TM) polarization is incident onto the prism. The waveguide and the coupling prism are rotated on a high precision motorized rotary stage on which they are mounted under computer-control. All the measurements were performed by using a single prism to determine the coupling angles of each mode. Initially, both symmetric trapezoid shape and right angle prisms made of SF-14 with base angles of 60^o were tried. Guided intensity is measured on the opposite side of the waveguide by a Si photodedector as a function of the incident angle. To minimize the noise, we used a lock-in amplifier which was connected to a computer that also controlled the rotary motor. From the angles, at which local intensity maxima are observed, the refractive index and thickness of the measured film can be obtained by solving the waveguide mode equations for TE and TM polarizations

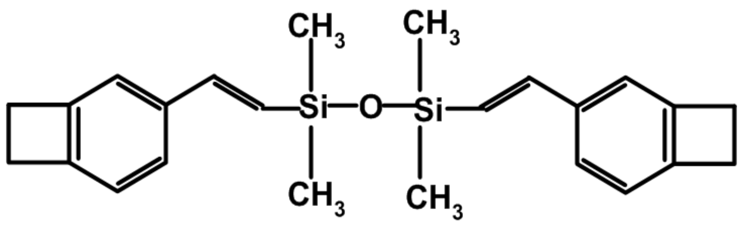

Figure 4. 11: Schematics of BCB monomer.

[38–40]. Attention must be paid towards properly aligning the coupling prism. The repeatability of the measured coupling angle has been checked and found to be less than $\pm$ 0.01^o. The intensity analysis method established in this study has been applied to obtain the refractive indices of the BCB thin polymer films. Typical error in the refractive index and thickness values was found to be less than $\pm$ 0.0002 and $\pm$ 0.3 %, respectively. All the experiments were carried out at a constant temperature of 21.0 $\pm$ 1.0 ^{o}C. The measured refractive index of BCB is 1.5575 at λ=632.8nm and 1.52at λ=1.55 μm.

Device Fabrication

Using EIM, a single mode waveguide, with BCB as the core material with SiO_2 as the cladding layer, was designed. BPM simulation was used to calculate the mode spectrum of the waveguide to confirm the single mode character. The single mode waveguide structure is shown in Figure 4. 8. Si substrate is used as a heat sink because of its high thermal conductivity. For bottom cladding 4 μm $\mathrm{SiO_2}$ layer is deposited with PECVD. Single mode waveguides fabricated with these design parameters were fabricated and found to be single mode. As described earlier, we prepared our polymer waveguide with cross-linked cyclotene polymer bisbenzocyclobutene (BCB) which is commercially available from DOW Chemical (Cyclotene 3022). Extent of cure and oxidation of the polymer is important for required optical properties. The polymerization of BCB is achieved by Diels Alder reaction [41]. Figure 4. 11 represent the BCB monomer, after polymerization highly cross-linked polymer network is established [41]. The extend of the curing reaction can be monitored by the growth of the band at 1500 cm^{-1} and by

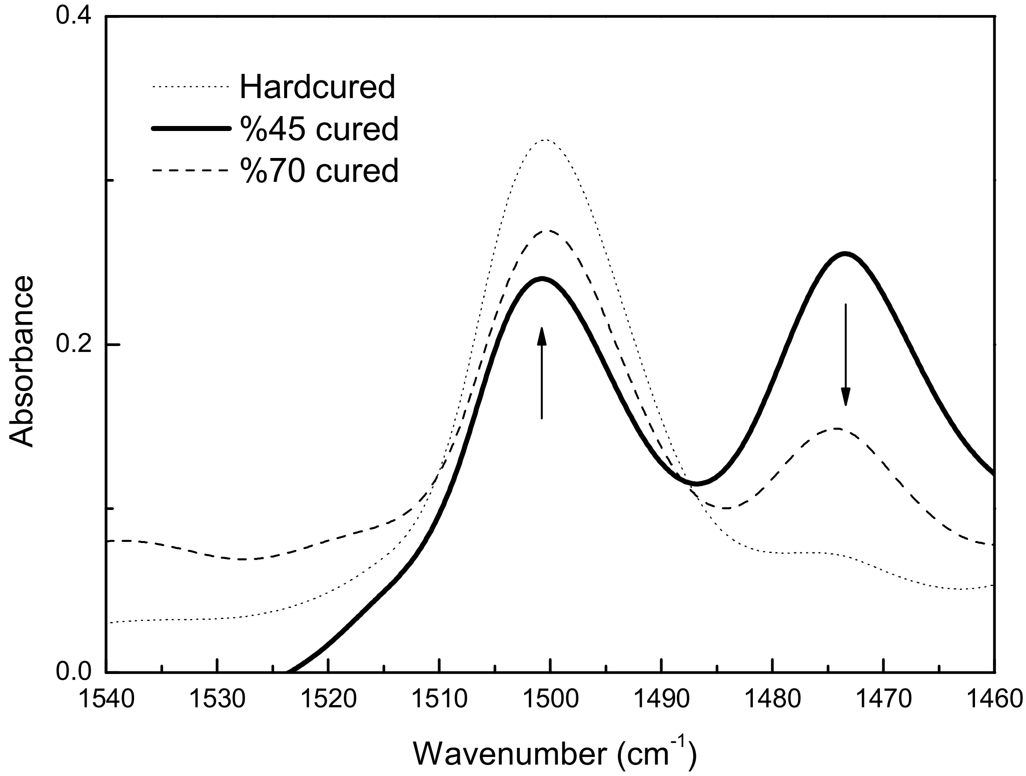

Figure 4. 12: Infrared spectrum of BCB film, at%45 ,%70 and hardcured .

the decrease in absorbance of 1475 cm^{-1} in the infrared spectrum, by using the widely-used spectroscopic technique, Fourier Transform Infrared spectroscopy (FTIR). Infrared absorption make use of the vibration of atoms in molecules. The spectrum is obtained by having radiation pass through a sample. The absorption features at particular energies, corresponding to the frequency of vibration of a molecule in structure of the film.

1500 cm^{-1} and 1475 cm^{-1} bands are associated with vibration of the tetrahydronaptalene polymerization products and motion of the four-membered cyclobutene reactant group, respectively. Several identical layers of BCB were spun on Si substrates. Typical changes in FTIR spectrum of BCB polymer were observed after curing at different temperatures. First one was cured at 150^{0}C for 30 min to achieve only solvent evaporation. Commercially available BCB is

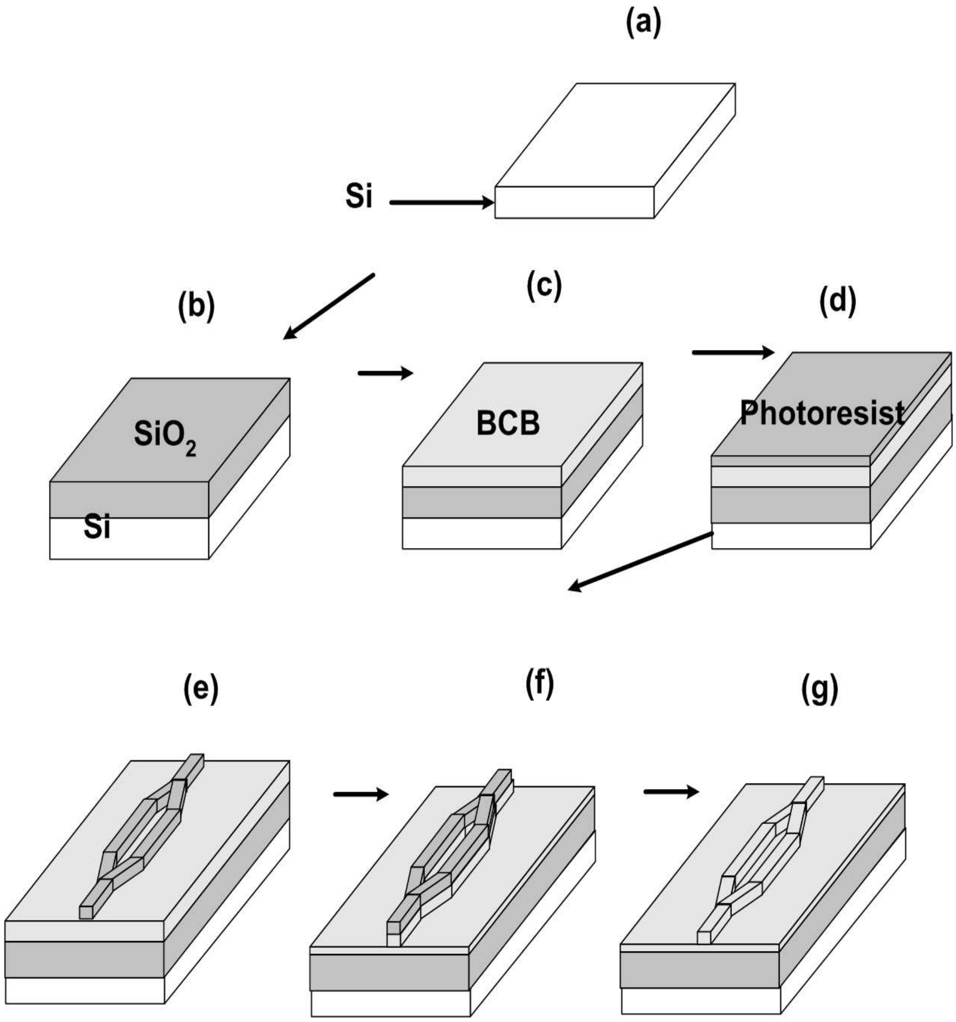

Figure 4. 13: Fabrication procedure of polymer waveguide,(a) Cleaned silicon substrate, (b) PECVD SiO_2 deposition, (c) BCB Spinning, (d) Photoresist spinning, (e) Photolithography, (f) RIE Etching, (g) Removing PR

partially polymerized (%45) and dissolved in mesitylene solution. Curing begins when the temperature exceeds $\sim 180\ ^0$C. So the curing extent of the first sample is approximately %45. Other samples were cured at 250 ^{0}C for 45 min. and 2 hours in a nitrogen atmosphere. The FTIR spectra for BCB films with different extent of cure are shown in Figure 4. 12. As shown in the figure that the absorption at 1500 cm^{-1} band increases and the absorption at 1475 cm^{-1} decreases when

CHF_3 Flow Rate	50 sccm
O_2 Flow Rate	20 sccm
Process Pressure	6 mTorr
RF Power	100W

Table 4.2: Process Parameters BCB RIE Etch.

curing extent increases. It is recommended in the literature that BCB films be cured under nitrogen atmosphere. During curing process, polymer product can be oxidized if the oxygen concentration is more than 100 ppm in the atmosphere.

Silicon is used as the substrate. In order to guide the light in the BCB layer a bottom cladding layer is required. First step in our device fabrication is SiO_2 deposition. The thickness of oxide layer was chosen as 4 μm so as to create sufficient optical insulation between silicon substrate and guiding layer. PECVD growth parameters for this process are listed in Table 3.2. BCB films were spin coated onto SiO_2 layer that are three solvent cleaned. Homogenous films with a transparent look are obtained with the spin speed of 5000 rpm. Immediately, after spin coating, and in order to prevent oxidation, films are polymerized in a closed oven in nitrogen environment. Full curing of BCB layers that are 2 um thick is achieved at 250 ^0C for 2 hours. This curing process is estimated to achieve curing of %95. The waveguide pattern can then be transferred through BCB film by using reactive ion etching (RIE) using standard photolithography techniques and using photoresist of 1.4 μm thickness as device mask. However, because of its silicon content, BCB can not be etched in pure oxygen plasma. Instead, 20:50 O_2:CHF_3 gas mixture was used to produce etch rate 660 ^{0}A/min. The RIE parameters used during the etching process are listed in Table 4.2. Remaining photoresist on the BCB layer is removed by rinsing in ACE. 4 μm SiO_2 layer is deposited by PECVD for upper cladding. And finally 0.25 μm Al is evaporated and using conventional lift-off process, heater is patterned. Figure 4. 13 illustrates the polymer waveguide fabrication. After facet cleavage sample is ready for optical measurements.

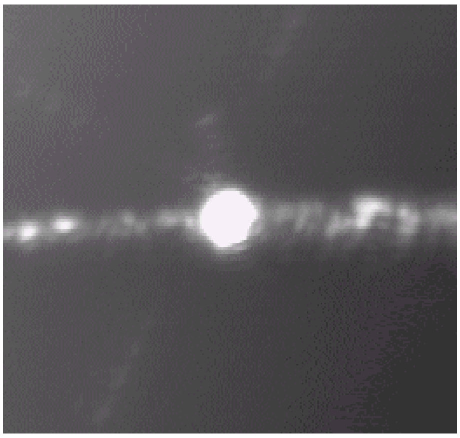

Figure 4. 14: View of TE_0 mode of Si based Y-junction MZ modulator as captured with IR camera.

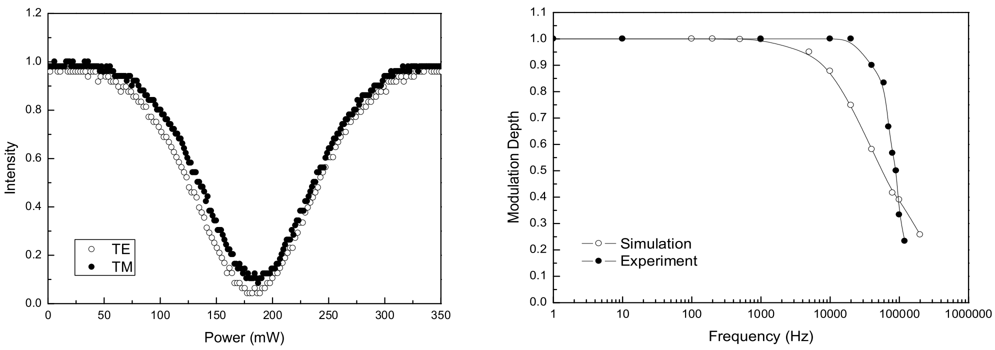

(a) (b)

Figure 4. 15: (a) Output intensity as a function of power. (b)Modulation depth vs. frequency for Si based MZI .

Results

The optical measurements are realized with butt coupling setup shown in Figure 3. 17. We first measured the operating power and amplitude modulation as a function of frequency for silicon based Y-junction modulator. As shown in Figure 4. 15, the required power for silicon based devices is 180 mW. Operating power is same for TE and TM measurements. It is higher than switching power of MMI

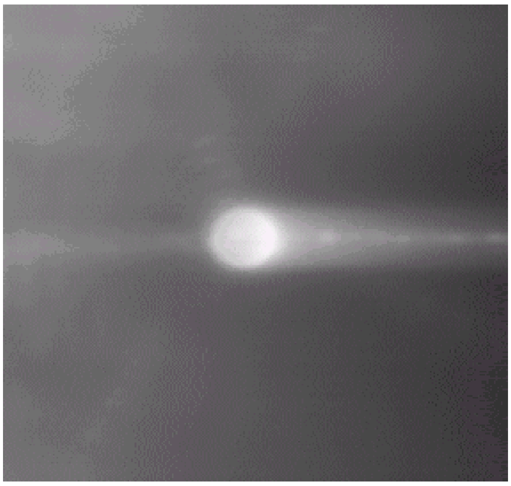

Figure 4. 16: View of TE_0 mode of polymer based Y-junction MZ modulator as captured with IR camera.

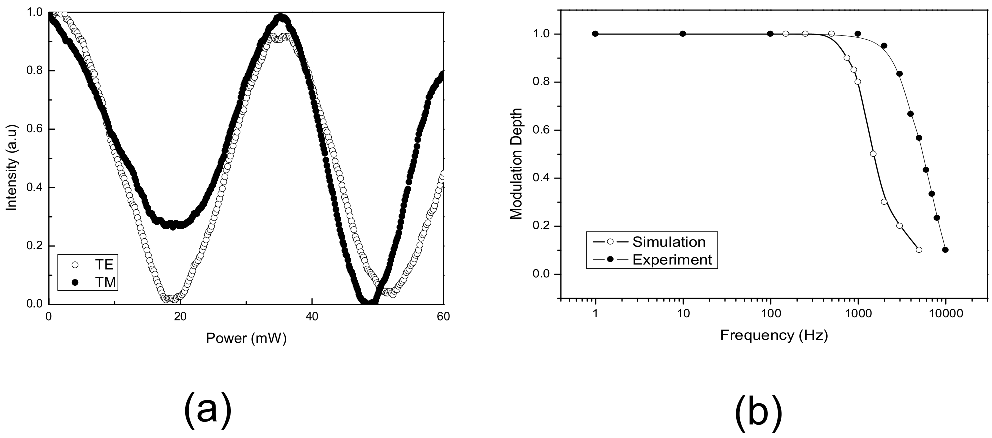

Figure 4. 17: (a) Output intensity as a function of power. (b)Modulation depth vs. frequency for polymer based MZI.

modulator because 2D heat diffusion increases amount of the required power. This power consumption can be decreased further by etching single or double trench at the both side of the heated waveguide.

The frequency response is also measured. The measured 3-dB cutoff frequency is 60 kHz. This frequency is suitable for provisioning and protection modulation in optical network applications. The FEM simulation also agrees with our measurement.

BCB based polymer Y- junction Mach Zehnder Modulators were also measured on the same setup. First, optical output intensity was measured as a function of applied electrical ramp for both TE and TM modes, separately as shown in Figure. 4.17a. It is clear from the figure that the device turns off at 18 mW and turns on again at 36 mW and turns off once more at 52 mW for TE mode. These results are similar for the TM mode. This indicates that the Ppi=18 mW. We note that TM mode does not approach to the minimum TE mode does at the first OFF position and requires slightly less power to turn OFF. Similar observations are made in the literature [32] and is attributed to possible higher order mode contributions or less than 3-dB splitting of the input power before it reaches the phase shifter region. Frequency response of this device to square wave pulses were also measured. A signal generator supplied the necessary pulses. Modulation depth as a function of frequency was monitored and the results are plotted in Fig 4.17b. The results obtained from FEM simulations are also plotted in the same graph. We observe that the modulator works with full ON/OFF up to 1 kHz beyond which the the modulation depth starts to decrease. We find that the 3-dB cut-off point is 5 kHz. This is one of the fastest devices for polymer thermo-optic Mach-Zehnder modulators available in the literature.

Chapter 5

Conclusions and Suggestions

Modulation of optical signal is an important issue in optical communications. Among the several mechanisms for modulation of optical signal, electro-optic modulation and thermo-optic modulation are mostly used. Even though electro-optic devices can operate at very high frequencies, they are usually polarization dependent and expensive due to the fact that electro-optic modulation requires noncentrosymmetric crystals, which are difficult to grow. Thermo-optic modulation, on the other hand, is present in most materials and therefore easy to implement in low cost materials. However, it has the disadvantage of being a slow process in comparison with electro-optic modulation.

In this work, we studied two different designs of Mach-Zehnder modulators based on silicon-on-insulator (SOI) and benzocylclobutane (BCB) polymer materials. We designed, fabricated and tested a MMI based Mach-Zehnder modulator and a Y-junction based Mach-Zehnder modulator on a SOI platform. Here, the core material is silicon with good optical and thermal properties. We have also designed, fabricated and tested a Y-junction based Mach-Zehnder modulator using BCB as the active medium .

The MMI Mach-Zehnder modulator on SOI platform was observed to have a turn off power (P_π) of 120 mW. FEM simulations of the same process produced P_π values of 114 mW. The agreement between FEM simulations and experimental values are remarkable. The high frequency response of the devices were also measured. The 3-dB cut-off of these devices were found to be as high as 60 kHz. These results are also supported by FEM simulations. These results are also in very good agreement with similar devices reported in the literature [32].

Y-junction Mach-Zehnder modulators have been fabrication both on SOI platform as well on Si substrate with BCB as the active core medium. The SOI device displayed a P_π of 180 mW as opposed to BCB based device where P_π is observed to be 18 mW. The difference can be explained in terms of the thermal properties of the materials involved. Si has much larger thermal conductivity as opposed to BCB and therefore requires higher heat input in order to achieve similar temperature induced index changes. This can be said in the light of the fact that the temperature dependent index changes for both BCB and Si are within the same order of magnitude.

The fact that Si has larger thermal conductivity becomes an advantage when it comes to high frequency modulation response of the devices. In response to square wave electrical power input, we find that 3-dB cut-off frequency for BCB based device is 5 kHz as opposed to 60 kHz for SOI based devices. We note, at this point, that while 5 kHz is small in comparison with SOI devices, it is nevertheless, the fastest device reported in the literature to the best of our knowledge. The only device that has the same or order of magnitude frequency response [36] requires cooling of the sample, a practical nuisance.

In conclusion, we have studied both MMI based and Y-junction based Mach-Zehnder modulators and obtained results in agreement with simulation and literature. We feel that our BCB based device is the fastest polymer device in the literature. More, however, can be done to improve upon our results. Including trenches about the phase shifter arms of Y-junction devices could lower P_π values even lower.

Bibliography

[1] Larry A. Coldren and Scott W. Corzine "Diode Lasers and Photonic Integrated Circuits" John Willey and Sons , 1995, New York, NY.

[2] G.P. Agraval and N.K. Dutta. "Long Wavelength Semiconductor Laser" Van Nostrand Reinhold,1986.

[3] C.Z. Zhao, E.K. Liu, G.Z. Li, L. Guo "Silicon on Insulator Optical Intensity Modulator Based on Waveguide Vanishing Effect" Electron. Lett. **32**(1996)1667-1668 .

[4] M.N. Khan, W. Yang, A. Gopinath. "Directional Coupler Electro-Optic Modulator in AlGaAs/GaAs with Low Voltage-Length Product " Appl. Lett. **62** (1993) 2033-2035.

[5] K.Komatsu, K.Hamoto, M. Sugimoto. "4×4 GaAs/AlGaAs optical Matrix Switches "J.Lightwave Technol. **9** (1991) 871-878.

[6] A. Bruce Buckman. "Guided-Wave Photonics" Sounders College Publisher(1992).

[7] C.M. Gee, G.D.Thurmond and H.W.Yen . "17 GHz Bandwidth electrto-Optical Modulator" Appl. Phys. Lett, (1983),**43**,998-1000.

[8] N. Goto, Y. Miyazaki, and K. Takahashi. "Dynamic Characteristics Analysis of Wavelength-Division-Multiplexing Guided-Wave Separation Switch Using Acoustooptic Effect" Jpn. J. Appl. Phys. **1-42**, 3041 (2003).

[9] Y.L. Liu, E.K. Liu, S.L. Zhang, G.Z. Li,J.S. Luo. "Silicon 1×2 Digital Optical Switch Using Plasma Dispersion" Electron Lett, (1994),**30-2**, 130-1.

[10] G. Cocorullo, I. Rendina . "Thermo-optical Modulation at 1,5 μm in Silicon Etalon " Electron Lett, (1992),**28-1**, 83-5.

[11] Rajiv Ramaswami, Kumar N.Sivarajan . "Optical Networks" Morgan Kaufmann Publisher, Inc. San Francisco, California.

[12] O. Mitomi, K. Noguchi, H.Miyazawa. "Ultra-Broadband and Low Driving Voltage $LiNbO_3$ Optical Modulators for Optical Transmission Systems" IEEE Lasers and Electro-Optic Society Annual Meeting, San Jose, CA, Oct.30-Nov. **2**,(1995) .

[13] Soref RA, Bennett BR. "Electrooptical Effects in Silicon " IEEE J Quantum Electron (1987), **23**,123-9.

[14] N. Keil, H.H. Yao. "Hybrid Polymer /Silica Thermo-optic Vertical Coupler Switches" Appl. Phys. B 73(2001), **73**,469-473.

[15] Mart B.J. Diemeer "Polymeric Thermo-optic Space Switches for Optical Communications",**6**, (1998) 192-200.

[16] H. Muller Physics,**6**, (1935) 176.

[17] R.M.Waxler et al. Appl. Opt. ,**18(1)**, (1997) 101-104.

[18] Christofer A. Long,"Essential Heat Transfer" Pearson, 1999, England

[19] H.S. Charslaw and J.C.Jaeger "Conduction of Heat in Solids" Oxford University Press, 1959, England

[20] Saeed Moaveni "Finite Element Analysis" Prentice Hall, 1999, New Jersey

[21] L.B. Soldano, and E.C.M. Pennings "Otical Multi-Mode Interference Devices Based on Self-Immaging: Princebles and Aplication" Journal of Lightwave Technology,**13:4**, (1995).

[22] D. Chen, H.R. Fetterman, A. Chen, W.H. Steier, L.R. Dalton, W. Wang, Y. Shi, "Demostration of 110 GHz electro-opticpolymer modulators" Appl. Phys. Lett. **70** (1997) 3335-3337.

[23] Clifford R.Pollock " Fundamentals of Optoelectronics" Richard D. Irvin,INC, 1995

[24] M.N. Khan, W. Yang, A. Gopinath, "Directionalcoupler electro-optic modulator in AlGaAs/GaAs with low voltage length product",Appl. Phys. Lett. **62**(1993) pp.2033-2035

[25] L.B. Soldano, A.H. de Vreede, M.K. Smit B.H. Verbeek E.G.Metall, and F.H.Groen,"Mach-zhender interferometer polarization splitter in InGaAsP/InP" IEEE Photon. Technol. Lett. **6**, (3) pp.402-405, 1994.

[26] U. Fischer, T. Zinke, B.Schüppert, K. Petermen, "Optical waveguide switch in silicon " Technical Digest, OEC '94, Chiba , Japan, pp. **15B3-5**

[27] R. Ulrish and G. Ankele, "Self-Imaging in Homogeneous Planar optical Wavegudes"Appl. Phys. Lett. **27:6** (1994)

[28] U. Fischer, T. Zinke, B. Schüpper and K. Petermann "Singlemode optical switches based on SOI waveguides with large cross-section " Electronic Letters 3rd March 1994 **30** (5)

[29] G.Cocorullo, M.Iodice, I.Rendina, and P.M. Sarro "Silicon Thermooptical Micromodulator with 700-kHz-3dB bandwidth" EEE Photon. Technol. Lett. **7**, (4) pp.363-365, 1995

[30] K.E. Bean "Anisotropic Etching of Silicon" IEEE Transactions on Electron Devices, **ED-25:10**, (1978)

[31] Yasuhiro Hida, Hidakatsu Onose, and Saburo Imamura "Polymer Waveguide Thermooptic Switch with Low Electric Power consumption At 1.3μm" IEEE Photon. Technol. Lett. **5**, (7) pp.782-784, 1993.

[32] U.Fischer, T.Zinke, K.Petermann "Integrated Optical Waveguide Switches in SOI " Proceedings 1995 IEEE International SOI Conference Oct.1995.

[33] Francisco Sircilli, Marcos A.R.Franco, AngeloPassaro and Nancy M.Abe "Finite Element Analysis of Thermo-optic Integrated Photonic Devices " Proceedings 2001 SBMO/IEEE MTT-S IMOC.

[34] S. Sohma, T.Goh, H.Okazaki, M.Okuna and A.Sugita "Low Switching Power Silica Based Super High Delta Thermo-optic Switch with Heat Insulating Grooves" Electronics Letters 31st January 2002 **38** (3)pp.127-128.

[35] A.Sugita, K.Jingiji, N.Takato, K.Katoh, and M.Kavachi "Bridge Suspended Silica-Waveguide Thermo-Optic Phase Shifter and Its application to Mach-Zehnder Type Optical Switch" Trans.IEICE,**E73**, (1) pp.105-109,Jan. 1990.

[36] R.Moosburger, and K.Petermann "4x4 Digital Optical matrix Switch Using Polymerik Oversized Rib Waveguide" IEEE Photonics Technology Letters, **10**, (5) pp.684-686 1998

[37] P. K. Tien "Light waves in thin films and integrated optics" , Appl. Opt., **10**, 2395, (1971).

[38] F. Michelotti, T. Gabler, H. Horhold, R. Waldhousl, A. Brauer: Optics Comm. **114**, 247 (1995).

[39] P. H. Chantome, L. Escoubas, F. Flory: Appl. Optics **41**, 3127 (2002).

[40] D.L. Lee: *Electromagnetic Principles of Integrated Optics* (Wiley, New York 1986).

[41] Dow Chemical Technical Data Sheet for BCB.